Article

Cell Reports

The FTLD Risk Factor TMEM106B Regulates the Transport of Lysosomes at the Axon Initial Segment of Motoneurons

Graphical Abstract

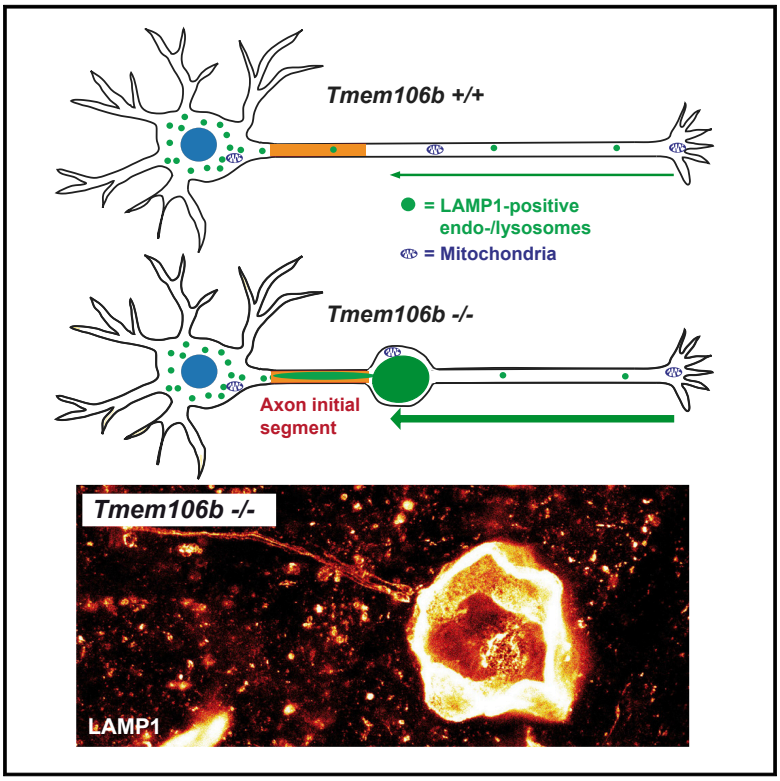

Highlights

- *Tmem106b* knockout leads to LAMP1-positive vacuoles at the axon initial segment
- Vacuolization is mostly confined to motoneurons
- Vacuoles develop due to impaired axonal trafficking of LAMP1-positive organelles
- Degradation of autophagic cargo is impaired due to TMEM106B deficiency

Authors

Patrick Lüningschrör, Georg Werner, Stijn Stroobants, ..., Bernd Knöll, Anja Capell, Markus Damme

Correspondence

mdamme@biochem.uni-kiel.de

In Brief

Genetic variants in the *TMEM106B* gene, coding for a lysosomal transmembrane protein, are linked to various neurodegenerative diseases. The function of TMEM106B remains enigmatic. Lüningschrör et al. analyze *Tmem106b*-knockout mice and find drastically enlarged LAMP1-positive vacuoles in proximal axons of selected motoneuron nuclei. Vacuolization is caused by impaired axonal transport.

Lüningschrör et al., 2020, Cell Reports *30*, 3506–3519
March 10, 2020
https://doi.org/10.1016/j.celrep.2020.02.060

CellPress

OPEN ACCESS
CellPress

Cell Reports
Article

The FTLD Risk Factor TMEM106B Regulates the Transport of Lysosomes at the Axon Initial Segment of Motoneurons

Patrick Lüningschrör,[1,12] Georg Werner,[2,12] Stijn Stroobants,[3] Soichiro Kakuta,[4] Benjamin Dombert,[1] Daniela Sinske,[5] Renate Wanner,[5] Renate Lüllmann-Rauch,[6] Benedikt Wefers,[7,8] Wolfgang Wurst,[7,8,9,10] Rudi D'Hooge,[3] Yasuo Uchiyama,[4] Michael Sendtner,[1] Christian Haass,[2,7,10] Paul Saftig,[11] Bernd Knöll,[5] Anja Capell,[2] and Markus Damme[11,13,*]

[1]Institute of Clinical Neurobiology, University Hospital Wuerzburg, University of Wuerzburg, 97078 Wuerzburg, Germany
[2]Chair of Metabolic Biochemistry, Biomedical Center (BMC), Faculty of Medicine, Ludwig-Maximilians-Universität München, 81377 Munich, Germany
[3]Laboratory of Biological Psychology, KU Leuven, 3000 Leuven, Belgium
[4]Department of Cellular and Molecular Neuropathology, Juntendo University Graduate School of Medicine, Tokyo, Japan
[5]Institute of Physiological Chemistry, Ulm University, 89081 Ulm, Germany
[6]Institute for Anatomy, Kiel University, 24098 Kiel, Germany
[7]German Center for Neurodegenerative Diseases (DZNE) Munich, Munich, Germany
[8]Institute of Developmental Genetics, Helmholtz Zentrum München, German Research Center for Environmental Health, 85764 Neuherberg, Germany
[9]Technische Universität München-Weihenstephan, 85764 Neuherberg/Munich, Germany
[10]Munich Cluster for Systems Neurology (SyNergy), 81377 Munich, Germany
[11]Institute of Biochemistry, Kiel University, 24098 Kiel, Germany
[12]These authors contributed equally
[13]Lead Contact
*Correspondence: mdamme@biochem.uni-kiel.de
https://doi.org/10.1016/j.celrep.2020.02.060

SUMMARY

Genetic variations in *TMEM106B*, coding for a lysosomal membrane protein, affect frontotemporal lobar degeneration (FTLD) in *GRN*- (coding for progranulin) and *C9orf72*-expansion carriers and might play a role in aging. To determine the physiological function of TMEM106B, we generated TMEM106B-deficient mice. These mice develop proximal axonal swellings caused by drastically enlarged LAMP1-positive vacuoles, increased retrograde axonal transport of lysosomes, and accumulation of lipofuscin and autophagosomes. Giant vacuoles specifically accumulate at the distal end and within the axon initial segment, but not in peripheral nerves or at axon terminals, resulting in an impaired facial-nerve-dependent motor performance. These data implicate TMEM106B in mediating the axonal transport of LAMP1-positive organelles in motoneurons and axonal sorting at the initial segment. Our data provide mechanistic insight into how TMEM106B affects lysosomal proteolysis and degradative capacity in neurons.

INTRODUCTION

Genetic variants in TMEM106B have been linked with differential aging and various neurodegenerative diseases, including frontotemporal lobar degeneration (FTLD), limbic-predominant age-related TDP-43 encephalopathy (LATE), and Parkinson's disease (Nelson et al., 2019; Tropea et al., 2019; van der Zee et al., 2011). The precise molecular function of TMEM106B is, however, still enigmatic. *TMEM106B* encodes a glycosylated lysosomal membrane protein with one transmembrane domain and type II topology (Lang et al., 2012). While the larger glycosylated carboxy-terminus faces the lysosomal lumen, the 96-amino-acid-long amino-terminus is localized in the cytosol. TMEM106B may play a role in the transport of lysosomes, based on studies in HeLa cells and cultured neurons (Clayton et al., 2018; Schwenk et al., 2014; Stagi et al., 2014). Overexpression of TMEM106B in neuronal and non-neuronal cells leads to TMEM106B dose-dependent enlarged dysfunctional lysosomes, as shown in several studies (Brady et al., 2013; Busch et al., 2016; Chen-Plotkin et al., 2012; Lang et al., 2012), though the molecular mechanism(s) explaining this effect remains to be determined. Acute knockdown of TMEM106B in HeLa cells causes a redistribution of lysosomes from the cell periphery to the perinuclear region (Schwenk et al., 2014) and a reduced number of lysosomes per cell (Stagi et al., 2014). In cultured primary hippocampal neurons, knockdown of TMEM106B affects the transport of lysosomes in dendrites, ultimately leading to reduced dendritic branching (Schwenk et al., 2014; Stagi et al., 2014). TMEM106B-deficient mice were generated and characterized previously (Arrant et al., 2018; Klein et al., 2017; Nicholson et al., 2018). Generally, no spontaneous phenotype in the basal TMEM106B-deficient situation was found except for subtle changes of lysosomal proteins, a downregulation of subunits of the V-ATPase, and decreased LysoTracker staining in primary cortical neurons (Klein et al., 2017).

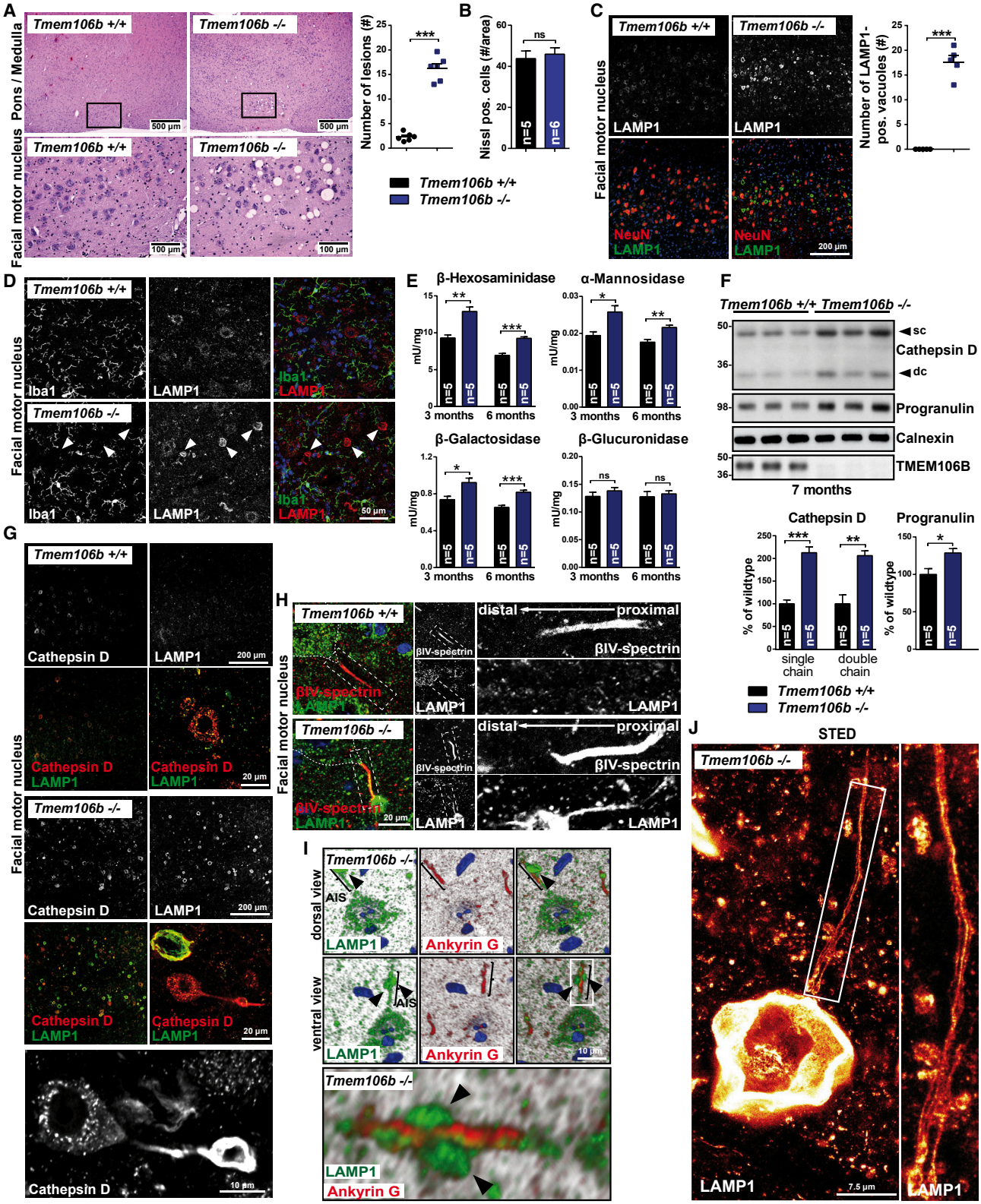

(legend on next page)

Genetic variants were first linked genetically with FTLD (Van Deerlin et al., 2010), the second most common form of presenile dementia, affecting up to 15 in 100,000 people at 45–64 years of age (Ratnavalli et al., 2002). Even though the precise mechanisms leading to neuronal dysfunction and, finally, cell death remain poorly understood, accumulating evidence hints to a dysfunctional endo-/lysosomal pathway (Ghazi-Noori et al., 2012; Götzl et al., 2014; Shi et al., 2018). The second most common cause of familial FTLD are heterozygous missense and nonsense mutations in *GRN*, coding for progranulin. Progranulin haploinsufficiency considerably increases the risk of developing FTLD (Baker et al., 2006; Cruts et al., 2006; Gass et al., 2006). Genetic approaches aiming to identify risk factors and modifiers for disease onset and severity by genome-wide association studies (GWASs) revealed the *TMEM106B* locus that segregates with the disease (Van Deerlin et al., 2010). Stratification of the patients highlighted a significantly reduced association of the *TMEM106B* "protective" allele with *GRN* carriers compared to non-*GRN* carriers. This genetic linkage of *TMEM106B* with FTLD and *GRN*-mutation carriers was validated in follow-up studies (Finch et al., 2011; Pottier et al., 2018; Premi et al., 2017; van der Zee et al., 2011). Subsequently, the *TMEM106B* protective allele was shown to be significantly associated with lower disease risk in *C9orf72* carriers (Gallagher et al., 2014; Premi et al., 2017; van Blitterswijk et al., 2014). In conclusion, *TMEM106B* is a bona fide risk factor and modulator for FTLD.

To gain insight into TMEM106B-dependent cellular processes, we generated *Tmem106b* knockout (KO) mice by CRISPR/Cas9 and independently by the homologous recombination of targeted embryonic stem cells (ESCs). TMEM106B-deficient mice present features affecting primarily motoneurons (MNs) of the facial motor nucleus (FMN) and other brain stem motor nuclei. MNs of *Tmem106b* KO mice show dramatically enlarged LAMP1-positive vacuoles specifically at the axon initial segment (AIS) and an increased retrograde axonal transport of lysosomes, implicating a pivotal role for TMEM106B in axonal transport in distinct neuronal populations and, as a consequence, impaired axonal autophagy. This phenotype was also observed in a second, fully independent *Tmem106b* KO mouse strain. Our results provide mechanistic insight into how TMEM106B may affect lysosomal proteolysis.

RESULTS

Deficiency of TMEM106B in Mice Leads to Vacuolization of Brain Stem Nuclei

Using CRISPR/Cas9-mediated genome editing, we generated TMEM106B-deficient mice by introducing short frameshift mutations in exon 3, the first coding exon (Figures S1A–S1D). Immunoblotting of brain and spinal cord lysates validated the complete absence of the detectable TMEM106B protein in homozygous KO mice and a reduction to ~50% in heterozygous animals (Figure S1E). Homozygous *Tmem106b* KO mice were born according to Mendelian frequencies after mating heterozygotes (Figure S1F). Adult *Tmem106b* KO mice had a similar weight to wild-type mice at an age of 10 weeks (Figure S1G). The major peripheral organs were unremarkable. Histologic analysis revealed spongiform vacuolization of selected brain areas at 10 weeks of age (Figures 1A and S2A). Spongiform vacuolization was particularly pronounced in the FMN but was also detectable in subregions of the thalamus, the trigeminal motor nucleus, and the hypoglossal nucleus. Vacuoles were regularly, but less frequently, seen in the anterior horn of the spinal cord (Figure S2A). The number of MNs in the FMN did not reveal differences between KO animals and controls even at 22 weeks of age (Figure 1B). Since TMEM106B is a lysosomal protein and TMEM106B overexpression leads to enlarged lysosomes in cultured cells (Brady et al., 2013; Chen-Plotkin et al., 2012; Gallagher et al., 2017; Stagi et al., 2014), we analyzed lysosomes in more detail. Immunofluorescence staining for the lysosomal marker LAMP1 revealed intensely stained, large round or infolded structures in the FMN, trigeminal motor nucleus, and thalamus of *Tmem106b* KO mice resembling the number, distribution, and size of the vacuoles seen by hematoxylin/eosin (H&E) staining (Figures 1C and S2B). Analysis of *Tmem106b* KO animals at different ages revealed first a solid appearance at 4 weeks of age, while 2-week-old animals barely showed any vacuoles, indicating that vacuoles are not due to defects in embryonic development (Figure S2C). The vacuoles stained negatively for the mitochondrial-marker Cox-IV (Figure S2D). Furthermore, these vacuoles did not represent phagosomes of microglia/macrophage origin, as revealed by Iba-1 co-staining. Neither signs of microgliosis nor astrogliosis were observed in

Figure 1. Accumulation of Drastically Enlarged Vacuoles of Lysosomal Origin in the AIS of the FMN

(A) H&E staining of the hindbrain and the FMN of 5-month-old control and *Tmem106b* KO mice. The number of vacuoles per FMN of individual animals is plotted (mean ± SEM, n = 6).

(B) Number of FMN Nissl-positive MNs in 6-month-old control and *Tmem106b* KO mice (mean ± SEM, n = 5–6).

(C) Immunofluorescence staining of the FMN with antibodies against LAMP1 (white, top panel; green, bottom panel) and NeuN (red, bottom panel) in 4-month-old mice.

(D) Immunofluorescence of Iba1 (green) and LAMP1 (red) of the FMN. Maximum intensity *Z*-projection of confocal stacks. Nuclei are stained with DAPI (blue). Age: 4 months.

(E) Enzymatic activity of the lysosomal hydrolases β-hexosaminidase, α-mannosidase, β-galactosidase, and β-glucuronidase in brain extracts of 3- and 6-month-old control and *Tmem106b* KO mice (mean ± SEM, n = 5).

(F) Immunoblots from brain lysates of 6-month-old mice for CatD progranulin, TMEM106B to confirm the KO, and calnexin to confirm equal loading. CatD and progranulin levels were quantified and normalized to wild-type mice (mean ± SEM, n = 5). dc, double-chain CatD; sc, single-chain CatD.

(G) Immunofluorescence of LAMP1 (green) and CatD (red) of the FMN. Nuclei are stained with DAPI (blue). Age: 4 months.

(H) Immunofluorescence of LAMP1 (green) and βVI Spectrin (red) of the FMN. The dashed box is shown enlarged. The soma of the MN is encircled with a dashed line. Nuclei are stained with DAPI (blue). Age: 4 months.

(I) Maximum intensity *Z*-projection of confocal stacks of LAMP1 (green) and AnkyrinG (red) staining of the FMN. Vacuolated lysosomes are marked by arrowheads. Nuclei are stained with DAPI (blue). Age: 4 months.

(J) LAMP1 immunofluorescence STED-microscopy image of an FMN vacuole. Age: 4 months.

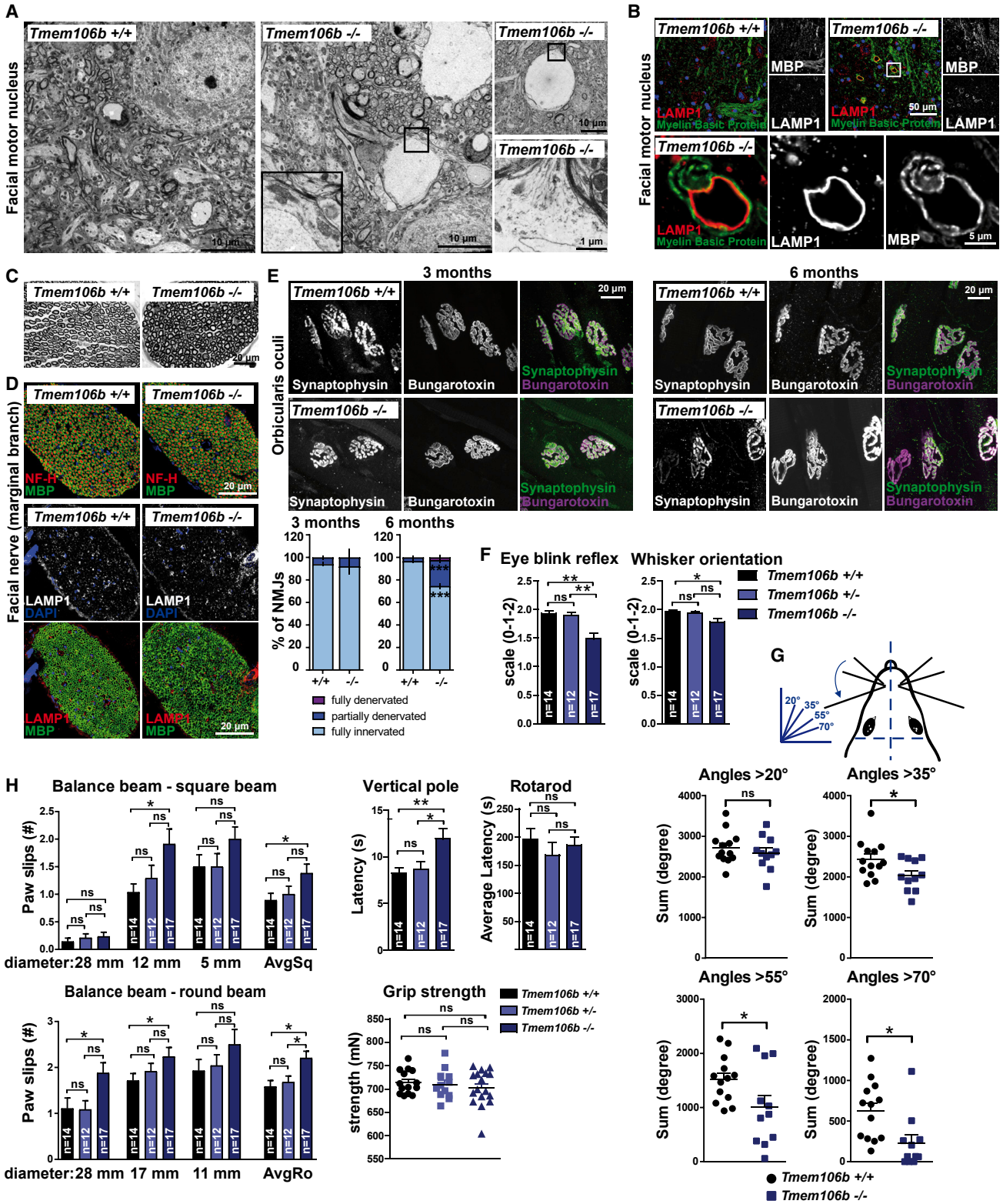

Figure 2. Axonal Vacuolization of the Facial MN Is Restricted to the Proximal Axon and Leads to Functional Facial Motor Deficits

(A) Electron micrographs of the FMN of 4-month-old wild-type and *Tmem106b* KO mice. Representative axons are shown. The boxed area is shown enlarged.

(B) Immunofluorescence staining of the FMN with antibodies against LAMP1 (red) and MBP (green). Nuclei are stained with DAPI (blue). Age: 4 months. The boxed area is shown enlarged.

(legend continued on next page)

the heavily vacuolated FMN at 4 months of age, as detected by immunofluorescence staining for Iba-1, CD68, and GFAP (Figures 1D and S2E). LAMP1-positive vacuoles in the FMN varied in size ranging from 1 μm to 35 μm, thus even partially exceeding the average size of MN somata. The activity of the lysosomal hydrolases β-hexosaminidase, α-mannosidase, and β-galactosidase, but not that of β-glucuronidase, was significantly increased in brain extracts of both 3- and 6-month-old *Tmem106b* KO animals (Figure 1E), while their transcript levels were unchanged (Figure S2F). Cathepsin D (CatD) levels in brain extracts were 2-fold increased in the *Tmem106b* KO animals, and progranulin expression was also significantly increased (Figure 1F). Since LAMP1 is not only present on lysosomes, but also found on other organelles from the endocytotic pathway, we further examine the identity of the LAMP1-positive vacuoles by staining with CatD as a marker of mature lysosomes. Co-staining of CatD and LAMP1 revealed a similar but not completely overlapping pattern of the vacuoles within the FMN (Figure 1G). Notably, CatD staining was also ring-like and did not fill the lumen of the vacuoles, but it often contained a "shaft"-like projection (Figure 1G, bottom panel). Most vacuoles showed immunoreactivity for both CatD and LAMP1 to a variable extent, but LAMP1-negative vacuoles were generally rare. We observed a general tendency of LAMP1-positive vacuoles being larger than CatD-positive vacuoles (Figure 1G). Next to the CRISPR/Cas9-mediated KO strain, we generated a second, independent *Tmem106b* KO mouse line by blastocyst injection of *Tmem106b*-targeted (ESCs) containing an artificial splice-acceptor site and β-galactosidase-containing reporter construct under the control of the endogenous *Tmem106b* promoter targeting exon 4, which is flanked by Cre- and flippase recombinase sites (tm2a allele). The KO in tm2a mice is based on efficient usage of the splice acceptor site, which is often leaky, leading to hypomorphic mice (Mitchell et al., 2001). To generate full KOs, tm2a-heterozygous animals were bred with Cre-recombinase-expressing mice, leading to a deletion of exon 4 and a frameshift in the coding region after exon 4 (tm2b allele) (Figures S3A–S3G). We used heterozygote tm2b animals to follow the expression of *Tmem106b* by X-gal staining, which showed a broad and ubiquitous expression throughout the brain, with a staining pattern resembling the general distribution of neurons (Figure S3C). Consistent with the CRISPR/Cas9 *Tmem106b* KO mouse line, this second, fully independent tm2b mouse line showed LAMP1-positive vacuoles in a similar distribution, increased levels of CatD, but no changes in the transcript levels of *Ctsd*, *Hexb*, *Man2b1*, *Glb1*, and *Gusb* (Figures S3D–S3G).

The close proximity of the LAMP1-positive giant vacuoles to the soma in both *Tmem106b* KO strains prompted us to investigate a relationship to the AIS of affected MNs. Notably, the entire AIS (visualized by staining for AnkyrinG or βIV-spectrin) of facial MNs showed regularly intense LAMP1 immunoreactivity, and very often a vacuole appeared at the distal end of the AIS or bulged from the AIS (Figures 1H and 1I). The AIS of cortical neurons or hippocampal CA3-neurons, however, lacked such LAMP1-positive vacuoles (Figure S4A). Stimulated emission depletion (STED) super-resolution microscopy of MNs *in situ* revealed a single tubular LAMP1-positive organelle often filling out the entire AIS, culminating with a giant vacuole at the distal end (Figure 1J). Electron microscopy of the vacuolated FMN revealed an electron-lucent character of the vacuoles. They were limited by a single membrane and were usually localized in the AIS or in myelinated axons, squeezing the remaining axoplasm between the vacuole membrane and axolemma (Figure 2A). However, organelles like mitochondria were regularly observed between the vacuoles and the axolemma, indicating that organelles are probably still able to pass these "roadblocks" (Figure 2A). More than one vacuole in a single axon was concomitantly observed, and the axon extended after a vacuole, indicating no axonopathy due to vacuolization (Figure 2A). This finding was confirmed by co-staining of LAMP1 with Tuj1 for visualization of the axon and a 3D reconstruction of *Z* stacks (Figure S4B). Immunofluorescence staining for Myelin basic protein (MBP) and LAMP1 verified the localization of the vacuoles in myelinated axons (Figure 2B). Correlative light-electron microscopy additionally confirmed the appearance of CatD at the limiting membrane of the vacuoles (Figure S5A).

Facial-Nerve-Innervated Muscle Groups Are Functionally Impaired in TMEM106B-Deficient Mice

Since proximal FMN axons are severely affected by vacuolization, we investigated the distal facial-nerve- and FMN-innervated neuromuscular junctions (NMJs) of the *orbicularis oculi* muscle in more detail and analyzed FMN-dependent behavioral changes as a functional readout. The peripheral facial nerve of *Tmem106b* KO mice was unaffected by vacuolization and appeared normally myelinated, as revealed by histology and immunofluorescence for MBP and neurofilament H (NFH) at the age of 5 months. Moreover, LAMP1-positive vacuoles were absent in the peripheral facial nerve (Figures 2C and 2D), the compact facial nerve in the hindbrain (Figure S2G), and the corresponding NMJ (Figure S2H). NMJs revealed a normal distribution and number of

(C) Toluidine blue-stained sections of the facial nerve (buccal branch) of a 4-month-old *Tmem106b* KO mouse and wild-type control.
(D) Immunofluorescence staining of the facial nerve (buccal branch) of a 4-month-old *Tmem106b* KO mouse and wild-type control for NFH (red), MBP (green), LAMP1 alone (white), or LAMP1 (red) and MBP (green). Nuclei are stained with DAPI (blue).
(E) Immunofluorescence staining of neuromuscular junctions (NMJs) of the *orbicularis oculi* muscle of 3- and 6-month-old *Tmem106b* and control animals with fluorescently labeled Bungarotoxin (magenta) and an antibody against synaptophysin (green). Quantification depicts the number of fully innervated or partially denervated NMJs of *Tmem106b* KO mice and wild-type controls (n = 3; 15–25 NMJs/animal).
(F) Quantification of the eye blink and whisker-orienting reflex in *Tmem106b*$^{+/+}$, *Tmem106b*$^{+/-}$, and *Tmem106b*$^{-/-}$ mice (n = 12–17). The average of six assessments was used for analysis. Three-point scale (0: absent; – 1: reduced; – 2: normal). Age: 2–3 months.
(G) Quantification of the whisker movement expressed as the addition of angles >20°, >35°, >35°, and >70° from *Tmem106b* KO and wild-type control mice. The sum in degree is depicted (n = 11–13; each point represents one animal; age: 6 months).
(H) Quantification of neuromotor function: number of paw slips during balance beam traversal (square and round beams), vertical pole latency, average rotarod latency, and grip strength of *Tmem106b*$^{+/+}$, *Tmem106b*$^{+/-}$, and *Tmem106b*$^{-/-}$ mice (age 2–3 months; mean ± SEM, n = 12–17).

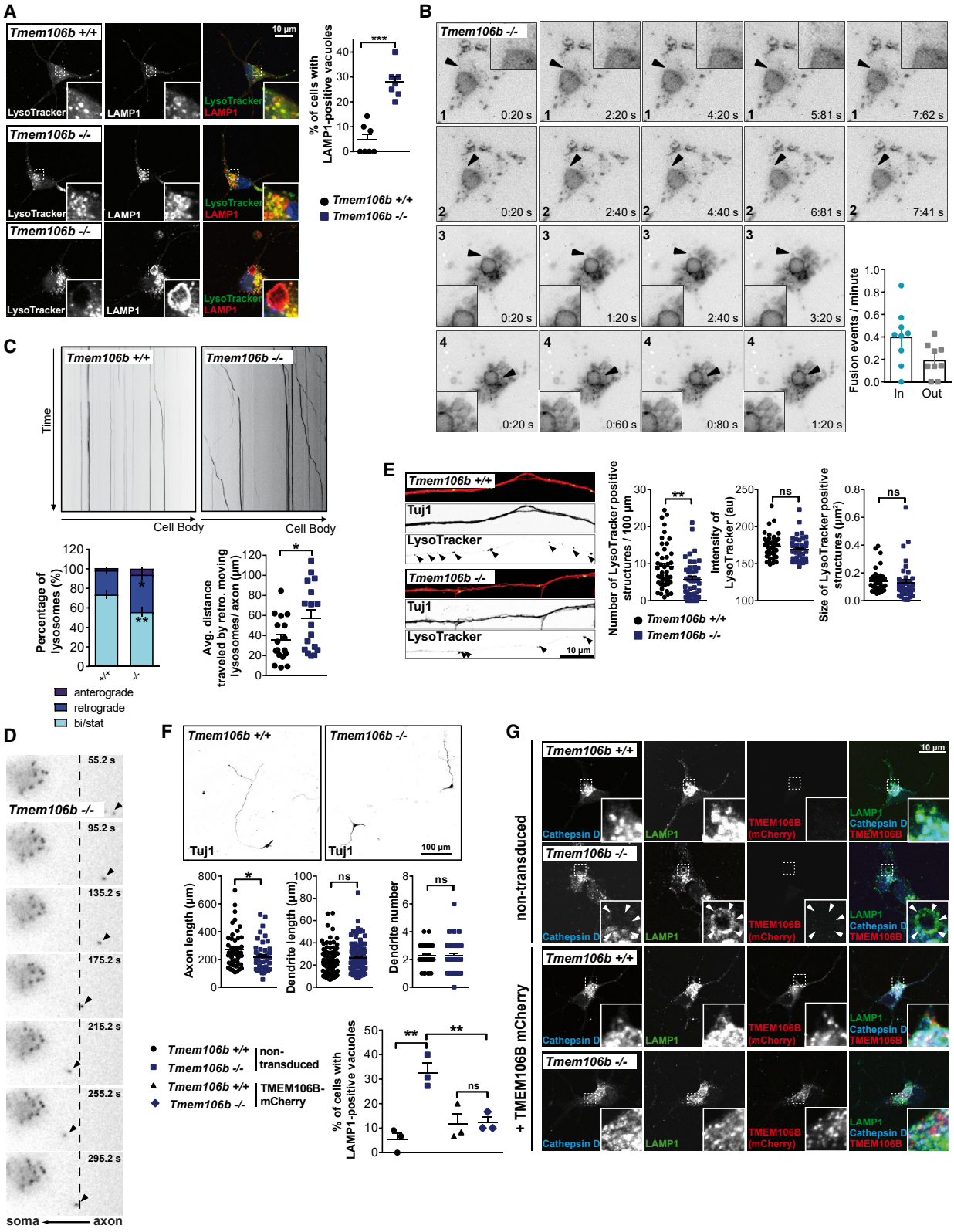

(legend on next page)

mitochondria and synaptic vesicles, as revealed by staining for Hsp60 and synaptophysin (Figure S2I). In 8- to 10-week-old mice, no signs of denervation or other pathologic alterations were observed for the NMJs within the *orbicular oculi* muscle in *Tmem106b* KO mice (Figure 2E). However, in 6-month-old animals, we detected a significantly enhanced number of partially denervated NMJs, as shown by synaptophysin staining. To a lesser extent, we also observed fully denervated axon terminals with a complete absence of synaptophysin (Figure 2E). Assessment of the eye blink reflex and whisker orientation—FMN-dependent motor groups—revealed a slight but significant reduced response of both muscle groups (Figure 2F). More sophisticated video-based tracking of the whisker movement measuring the total number of all angles and the total number of peaks (Figures 2G, S5B, and S5C) by counting the addition of angles, revealed significant differences between wild-type and *Tmem106b* KO mice at the age of 8–10 weeks for all angles >35°, implicating functional impairment of the corresponding innervating MNs. More general motor function tests revealed slightly reduced motor coordination in balance beam and vertical pole tests, but no significant differences in rotarod performance or grip strength. Heterozygous animals did not show significant differences (Figure 2H). Eye blink reflex and whisker orientation remained statistically significant between the genotypes in mice at 14 months of age, and there was a progressive decline in motor coordination, tested by the balance beam test (Figure S5D). These data indicate proximal nerve pathology in the absence of major myelination defects, leading to impaired MN function and accompanied by moderate and partially progressive behavioral deficits.

Retrograde Axonal Transport of Lysosomes Is Impaired in *Tmem106b* KO Mice

Our findings of LAMP1-positive vacuoles within proximal but not distal axons of MNs *in situ* encouraged us to investigate the axonal transport of lysosomes in primary MNs *ex vivo*. Even though vacuoles were less frequent, we routinely observed MN vacuolization *in situ* in spinal cord sections, as assessed by histology and co-staining with a ChAT antibody (Figures S2A, S2B, and S6A), implying that spinal MNs serve as a good model system.

In total, 28% of cultured MNs from TMEM106B-deficient (but not wild-type) mice showed LAMP1-positive vacuoles, mostly within the soma and to a much lesser extent in proximal axons, after 5 days *in vitro* (DIV5) (Figure 3A). Primary neurosphere-derived neurons from Tmem106b KO mice lacked such vacuoles (Figure S6B), emphasizing again that MNs are the primary affected neuronal cell type. LAMP1-positive vacuoles in primary MNs stained negative for LysoTracker and CatD, suggesting that they do not represent fully matured lysosomes (Figures 3A and S5C). Since we almost exclusively detected these vacuoles at the AIS *in situ*, we also stained for AIS markers in cultured MNs. In contrast to MNs *in situ*, cultured MNs seem not to have fully established an AIS, probably leading to the buildup of LAMP1-positive vacuoles at the soma. We wondered whether these structures are still active in terms of membrane exchange. Upon lentiviral expression of LAMP1-GFP, we specifically monitored LAMP1-positive vacuoles and analyzed fusion and/or fission events. Our data show that smaller LAMP1-GFP structures fuse with and bud off these large vacuoles (Figure 3B). Based on these experiments, we calculated the rate of fission and fusion events per minute and detected a higher number of fusing structures in comparison to structures budding off (Figure 3B). In summary, these experiments show that *in vitro*, the LAMP1-positive vacuoles still undergo membrane turnover, probably leading to the net growth of the vacuoles.

Although the LAMP1-positive vacuoles stained negative for LysoTracker, we wondered whether acidified organelles in axons were also affected in TMEM106B-deficient MNs. Live cell imaging and tracing of LysoTracker-labeled vesicles in the proximal axon of DIV7 MNs revealed a significantly higher percentage of retrograde transported LysoTracker-positive vesicles in KO cells than in wild-type control cells. Furthermore, retrograde moving LysoTracker-positive vesicles traveled an increased total distance in TMEM106B-deficient animals (Figure 3C). Intriguingly, LysoTracker-positive vesicles were frequently observed moving along the proximal axon but stopping before entering the soma and the very proximal part of the axon, implicating defects in the entry into the soma (Figure 3D; Video S1). In wild-type MNs, lysosomes traveled a shorter distance and were mostly stationary (Video S2). Furthermore, quantification of LysoTracker-positive vesicles in fixed cells revealed a similar size and LysoTracker intensity but a

Figure 3. Retrograde Axonal Sorting of Lysosomes Is Impaired *Ex Vivo* and *In Vivo*

(A) LysoTracker DND-99 (green) with LAMP1 (red) immunofluorescence-staining of DIV7 primary MNs. Two representative images of *Tmem106b* KO MNs are shown. Nuclei are stained with DAPI (blue).

(B) Single frames of two representative videos of lentiviral LAMP1-GFP-infected primary MNs of *Tmem106b* KO mice. Four representative independent fusion events of two different cells are shown. Quantification of organelles undergoing fusion or fission with the large LAMP1-positive vacuole. Single lysosomes are labeled with arrowheads.

(C) Kymographs of axonal LysoTracker-positive organelle movement in isolated MNs from control and *Tmem106b* KO mice (DIV7). Quantification of the directional movement and the total retrograde traveled distance are shown. n = 16–19 lysosomes per genotype/condition. Two representative images of *Tmem106b* KO MNs are shown.

(D) Single frames of a representative video of LysoTracker-stained MNs isolated from *Tmem106b* KO mice. A single lysosome is labeled with an arrowhead.

(E) LysoTracker DND-99 (green) with Tuj1 (red) immunofluorescence staining of axons (as in B) of DIV7 primary neurons. Quantification of the number of LysoTracker-positive organelles, intensity, and size per axon is shown (mean ± SEM, n = 12–16 cells/experiment; three experiments).

(F) Representative Tuj1 immunofluorescence-stained primary neurons (DIV7). Quantification of the axon length, dendrite length, and dendrite number. (mean ± SEM, n = 15–20 cells/experiment; three experiments).

(G) Immunofluorescence staining for LAMP1 (green) and CatD (blue) of lentiviral TMEM106B-mCherry (red) transduced or non-transduced primary cultivated MNs from control and *Tmem106b* KO mice (DIV7). A quantification of the number of cells with LAMP1-positive swelling is depicted (mean ± SEM, n = 3).

slightly decreased number in the axons of *Tmem106b* KO mice (Figure 3E). Next, we measured the dendrite number and dendrite and axon length in cultured MNs to address whether TMEM106B deficiency has any morphological consequences. We detected a slight but significantly decreased axon length but no differences in dendrite number or length in *Tmem106b* KO MNs (Figure 3F).

Finally, we performed a rescue experiment with primary MNs. Lentiviral re-expression of ubiquitin-driven mCherry-tagged TMEM106B in primary neurons fully rescued the presence of vacuoles in *Tmem106b* KO MNs, indicating that this phenotype is indeed due to a loss of function of TMEM106B (Figure 3G).

To investigate the axonal transport of endocytic organelles dynamically in facial MNs *in situ*, we applied the neuronal tracer FluoroGold (FG), which is frequently used for retrograde labeling experiments. FG is endocytosed and retrogradely transported in endo-/lysosomes finally reaching the MN soma (Schmued and Fallon, 1986). We first tested whether the endocytosis of FG differs between wild-type and *Tmem106b* KO primary MNs (Figure 4A), but we detected no difference in the endocytic uptake of FG after 15 or 60 min. Next, FG was injected into the FMN-innervated whisker pads of 4-month-old animals (Figure 4B), an age with established pathology. After perfusion and fixation of the mice 4 days after injection, sections were stained with an antibody against FG and LAMP1. In total, ~75% of all LAMP1-positive vacuoles were positive for FG, confirming our observation in cultured MNs that vacuoles are still active in terms of membrane fusion. Several LAMP1-positive vacuoles, especially small ones, stained intensively for FG, validating the axonal and endosomal origin of the vacuoles, while large vacuoles were partially FG negative (Figure 4C). Importantly, for a shorter period of 1 day after FG injection, both the number of FG-positive MNs and the total area of FG in the somata of the FMN were significantly reduced (Figure 4D). These findings provide further evidence that the accumulation of lysosomal membrane structures at the AIS is due to altered retrograde transport, resulting in an impaired delivery of lysosomes to the soma (Figure 4E). These data also suggest that TMEM106B deficiency affects MNs in a cell-autonomous manner, resulting in defective axonal transport of LAMP1-positive organelles and axonal outgrowth *in vitro* and defective retrograde transport of FG-positive vesicles *in vivo*.

TMEM106B Deficiency Causes Impaired Clearance of Lysosomal Cargo and Reduced Turnover of Autophagosomes

We next investigated in more detail whether the altered transport of LAMP1-positive organelles leads to an impaired turnover of axonal autophagosomes. To explore this in cultured MNs, we utilized a lentiviral vector coding for tandem-fluorescent-tagged RFP-GFP-LC3, allowing discrimination between acidified and non-acidified vesicles (Lüningschrör et al., 2017). Quantification of the number of autophagosomes and autolysosomes from DIV7 primary MNs showed an almost doubled number of axonal autophagosomes but a comparable number of autolysosomes in *Tmem106b* KO compared to wild-type MNs, implicating reduced fusion of autophagosomes with lysosomes (Figure 5A). As previously shown (Lüningschrör et al., 2017), in axons of primary MNs, autolysosomes were hardly detectable, suggesting that the final maturation into lysosomes takes place at the soma. To further investigate the interaction of autophagosomes with LAMP1-positive vacuoles in primary MNs, we simultaneously expressed LAMP1-GFP and RFP-LC3 in cultured MNs (Figure 5B). We specifically analyzed MNs containing LAMP1 vacuoles and found that the majority of vacuoles were LC3-RFP positive, suggesting that these vacuoles indeed fused with autophagosomes at a certain stage but failed to mature to genuine lysosomes, as shown by negative staining for CatD (Figure 3A). In this line, an increase of LC3 II (the autophagosome-bound lipidated form) was also observed in primary mouse embryonic fibroblasts (MEFs) of *Tmem106b* KO mice under basal conditions (Figure S7A). Inhibition of the fusion of lysosomes with autophagosomes in MEFs by bafilomycin A showed no further increase in LC3 II in the *Tmem106b* KO cells compared to the wild type, indicating no enhanced generation of autophagosomes, but an impaired fusion of lysosomes and autophagosomes in *Tmem106b* KO MEFs.

Immunoblots from brain extracts of 6-month-old wild-type and *Tmem106b* KO mice for LC3, p62, and ubiquitin revealed a significant increase in LC3 II, p62, and high-molecular-weight ubiquitinated proteins, further providing evidence for a pathological accumulation of autophagosomes and autophagic cargo/substrates (Figure 5C). In this line, large p62-positive aggregates were observed in the hindbrain and spinal cord of *Tmem106b* KO mice by immunofluorescence (Figure 5D). The p62-positive aggregates started to appear at 4 months of age and were very rarely seen in regions other than the hindbrain. We observed a slight but significant increase in the amount of autofluorescent neuronal lipofuscin in the thalamus (Figure 5E), an area also affected by vacuolization. Electron microscopic evaluation and quantification of the lysosomal volume density revealed a significant increase in the volume of lipofuscin-filled lysosomes in both the spinal cord and the thalamus, but not the cerebral cortex (Figure 5F). In support of the data of the CRISPR/Cas9-mediated *Tmem106b* KO mice, the *Tmem106b*^{tm2b} KO mice similarly showed an increase of LC3 II, high-molecular-weight ubiquitin aggregates, increased autofluorescence in the thalamus, and p62-positive aggregates (Figures S7B–S7D). These results point toward a reduced clearance of lysosomal substrates and autophagic cargo in *Tmem106b* KO neurons, possibly caused by altered axo-dendritic sorting of lysosomes.

DISCUSSION

The major phenotypic features of *Tmem106B* KO mice are giant LAMP1-positive vacuoles specifically occurring at the AIS of MNs. Vacuole formation ultimately leads to functional deficits of the affected motor units as a consequence of the loss of TMEM106B. The enlarged vacuoles are partially negative for CatD *in situ* and *in vitro* and negative for LysoTracker, but they are positive for LAMP1. Therefore, they do not represent genuine functional lysosomes. Even the designation of those highly non-physiological organelles as ''lysosomes'' should be taken with caution, as they might also represent late endosomes, autolysosomes, or hybrid organelles. However, as they bear no similarity to any physiological organelles in wild-type mice, a more precise designation is useless. In this regard, it should also be noted that

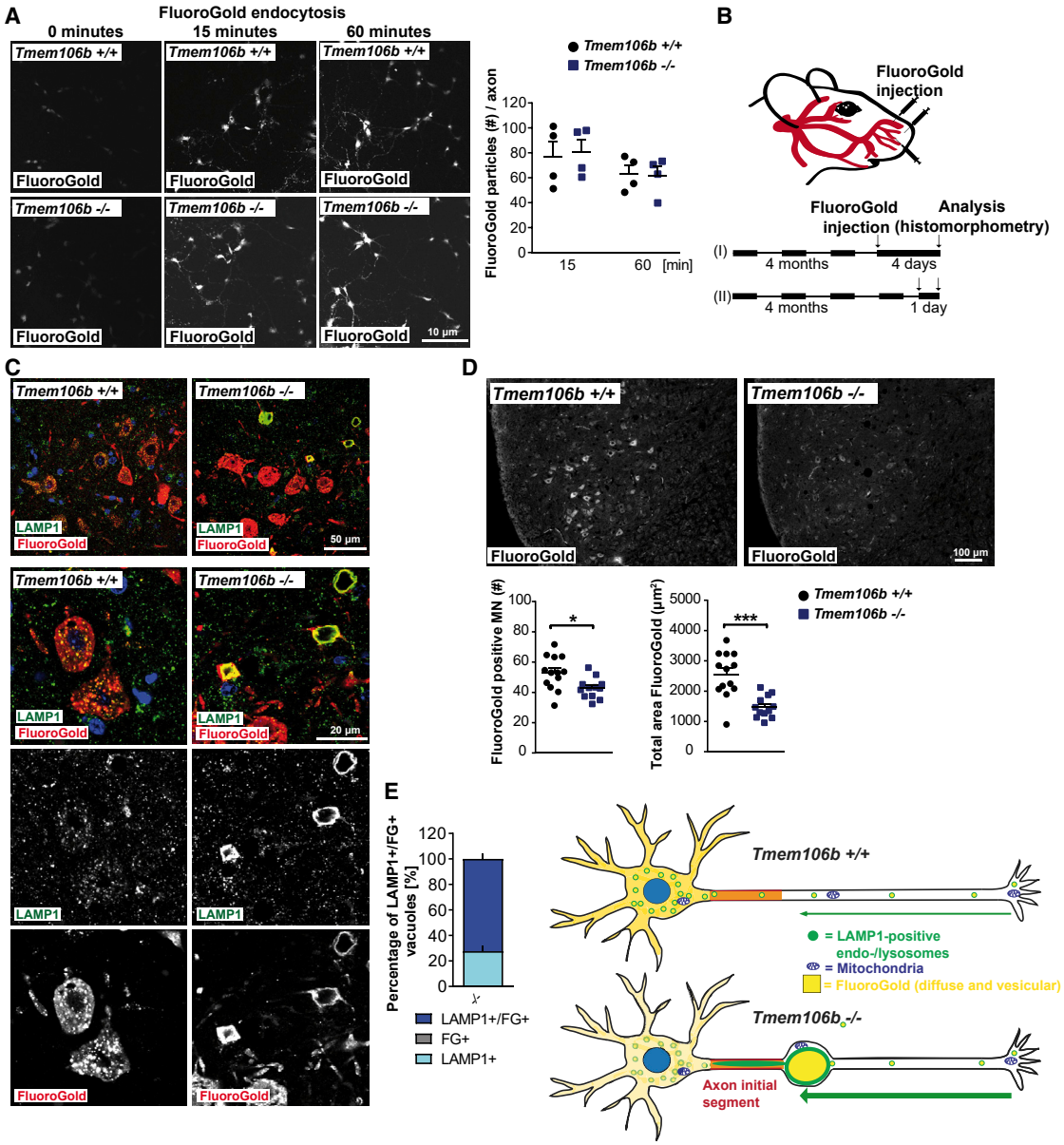

Figure 4. TMEM106B Deficiency Leads to Reduced Delivery of the Retrograde Tracer FluoroGold in MNs *In Vivo*

(A) Primary MNs from wild-type and *Tmem106b* KO mice (DIV5) were offered FluoroGold (FG) for 15 min, washed, and chased for the indicated time points. FG was stained by immunofluorescence with an FG-specific antibody. The number of FG particles in axons was counted and is depicted on the right. Somata were excluded from the analysis (mean ± SEM, n = 4).

(B) Scheme of the FG retrograde labeling experiments.

(C) Immunofluorescence of the FMN for FG (red) and LAMP1 (green) 4 days after FG injection. Nuclei are stained with DAPI (blue). Quantification of FG and/or LAMP1-positive vacuoles is depicted (n = 3).

(D) Representative image of the FMN stained for FG 1 day after injection of FG in wild-type control and *Tmem106b* KO mice (4 months). Quantification of the number of FG-positive MNs and area covered by FG staining is shown (mean ± SEM, n = 12–13).

(E) Scheme of the localization of LAMP1-positive organelles (green) in MNs of wild-type control and *Tmem106b* KO mice. The distribution of FG (yellow) is indicated.

LAMP1-positive organelles even in wild-type neurons represent a heterogeneous population of endocytotic organelles (including late endosomes and autolysosomes) that are processed toward degradative lysosomes (Cheng et al., 2018). Such LAMP1-positive organelles are enriched in axons and most likely contain retrogradely transported cargo derived from the distal axon like maturing autolysosomes/autophagosomes (Maday et al., 2014). The fact that most vacuoles in primary MNs were positive for LC3 indicates that autophagosomes significantly contribute to their biogenesis.

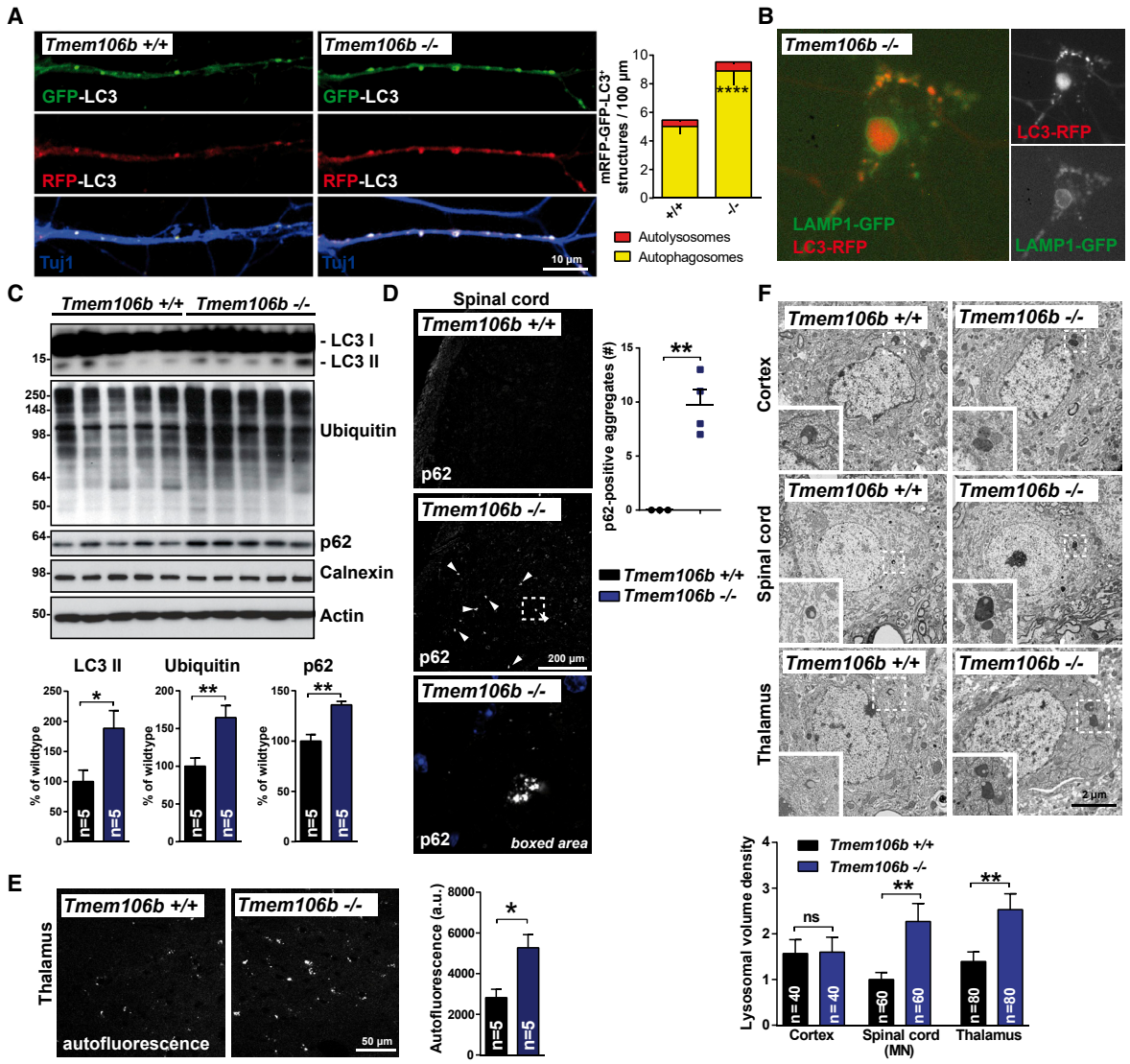

Figure 5. TMEM106B Deficiency Impairs the Degradation of Lysosomal Substrates

(A) Representative confocal images of the axon of lentivirus-infected tandem fluorescent-tagged LC3 (mRFP-EGFP-LC3)-expressing primary MNs (DIV7) of *Tmem106b* KO and control cells. RFP channel is depicted in red, GFP channel is depicted in green. The axon is stained with an antibody against Tuj1 (blue). Quantification of RFP-positive (autolysosomes) and RFP-GFP-double-positive organelles (autophagosomes) in the axon. Mean ± SEM; n = 10 neurons/experiment; three experiments; two-way ANOVA; Bonferroni post-test.

(B) Primary MNs (DIV7) of *Tmem106b* KO mice infected with lentiviruses coding for LAMP1-GFP (green) and LC3-RFP (red).

(C) Immunoblots of total-brain lysates with the indicated antibodies. Age: 6 months. Quantification is shown below. Mean ± SEM; n = 5.

(D) Immunofluorescence staining of the spinal cord for p62. p62-positive aggregates are marked with arrowheads. Quantification of the number of p62-positive aggregates/section (mean ± SEM, n = 3–4). Nuclei are stained with DAPI (blue). Age: 4 months.

(E) Representative confocal images of autofluorescence (488-nm laser excitation) in the thalamus of *Tmem106b* KO and control mice. Age: 4 months.

(F) Electron micrographs of neurons of the cortex, spinal cord, and thalamus. A quantification of lysosomal volume density is given. Mean ± SEM (n = 40–80 single neurons from two independent mice/genotype).

Three groups previously reported the generation and characterization of TMEM106B-deficient mice (Arrant et al., 2018; Klein et al., 2017; Nicholson et al., 2018). Interestingly, key phenotypic alterations described in the two KO strains described in our study (vacuolization of MNs, increased autophagosomes, and aggregates) were not reported. Generally, no spontaneous phenotype in the basal *Tmem106b* KO situation was found in previous studies except for subtle changes of lysosomal proteins like cathepsin B, cathepsin L, and DPP7; a downregulation of subunits of the V-ATPase; and decreased LysoTracker intensity in primary neurons. We, in contrast, observed an increase in the activity of several lysosomal enzymes and increased levels of

CatD. No major differences in the LysoTracker staining were observed in primary neurons. Notably, both previously published mouse models were generated by the same KO strategy: both strains are ''knock-in-/KO-first'' alleles, in which an intronic gene trap vector with an artificial splice-acceptor site abrogates the transcription of the wild-type transcript. However, this strategy might result in an incomplete KO: due to incomplete usage of the splice-acceptor site, the resulting mouse lines can be hypomorphs with residual wild-type transcript and protein instead of a full KO (Mitchell et al., 2001). In both studies, the authors crossed homozygous or heterozygous *Tmem106b* gene trap mice with progranulin KO mice and observed a partial rescue of the *Grn* KO phenotype (Klein et al., 2017; Arrant et al., 2018). If the *Tmem106b* KO was incomplete, the results of these experiments are also difficult to interpret. Alternatively, in the previous studies, the phenotype described here has not been detected because the histological characterization focused on brain regions more relevant for FTLD.

Overexpression of TMEM106B in cultured cells leads to enlarged dysfunctional lysosomes, as shown in several studies (Arrant et al., 2018; Brady et al., 2013; Chen-Plotkin et al., 2012; Gallagher et al., 2017; Lang et al., 2012), and TMEM106B knockdown leads to a reduced number of lysosomes (Chen-Plotkin et al., 2012; Stagi et al., 2014). Our observation of drastically enlarged, LAMP1-positive organelles in the KO situation appears to be counterintuitive in that regard. However, it seems to be plausible that the levels of TMEM106B need to be tightly balanced, and both reduced levels as well as increased levels cause dysregulation of lysosomal size. Whether both situations are caused by the same molecular mechanism(s), however, needs to be formally proven. In this respect, it should also be noted that the lysosome enlargement is dose dependent (Gallagher et al., 2017). These findings have relevance for TMEM106B's role in disease, given that the effect of genetic variants in different disease entities (e.g., on TMEM106B levels) is still obscure. In cultured primary hippocampal neurons, knockdown of TMEM106B affects the transport of lysosomes in dendrites (Schwenk et al., 2014). These studies were complemented by analyses with primary cortical neurons, showing a similar effect on the neuritic transport of lysosomes (Stagi et al., 2014). In both studies, an increase in the number of moving lysosomes was shown. However, it remained unclear whether TMEM106B knockdown affects the transport of moving lysosomes in the anterograde or retrograde direction in neurites, and both studies focused on moving lysosomes in dendrites. The availability of the new *Tmem106b* KO models allowed histopathological analyses of proximal and distal nerve segments and an unbiased survey of the loss-of-function effect in different terminally differentiated neuronal cell types. These *in vivo* data support a primary defect in lysosome positioning, and they clearly show that TMEM106B is particularly important in the sorting of lysosomes in the axon rather than in dendrites and that the retrograde movement is altered. The axon differs in several regards from dendrites: in contrast to dendrites, the axon contains a tight barrier, the AIS, which is preventing somatodendritic cargo from entering . If there are any gatekeeper mechanisms for retrograde cargo, controlling entry of cargo into the AIS from the distal end is unknown. Additionally, the orientation of microtubules considerably differs between the axon and dendrites: while the axon has a uniform arrangement of microtubules with plus ends distal to the cell body (plus-end out), dendrites have equal numbers of plus- and minus-end-out microtubules (Yau et al., 2016). Both features might contribute to the observed phenotype with an accumulation of large LAMP1-positive vacuoles at the distal AIS. Finally, the cargo (i.e., the LAMP1-positive organelles) differ in their microtubule-interacting motor machinery between dendrites and the axon, contributing to differences between dendritic and axonal sorting. Knockdown of TMEM106B in primary cortical neurons was previously shown to increase the retrograde transport of lysosomes in dendrites (Schwenk et al., 2014). This effect might be even more pronounced *in vivo* and in MNs with their long complex axon, ultimately explaining the observed phenotype. Interestingly, a recent study revealed altered positioning of endo-/lysosomes in dendrites of cortical neurons of CHMP2B-deficient mice (Clayton et al., 2018), which were previously shown to develop axonal degeneration as well (Ghazi-Noori et al., 2012). This altered positioning of lysosomes in dendrites of CHMP2B-deficient mice was rescued by knockdown of TMEM106B (Clayton et al., 2018). It will be interesting to determine if TMEM106B levels also affect axonal degeneration in CHMP2B-deficient mice.

The observation that cultured spinal MNs frequently show LAMP1-positive vacuoles in both the soma and the proximal axon suggests that an impaired transport of lysosomes is cell autonomous and is the primary cause for the observed phenotype, and impaired autophagy and formation of vacuoles is a secondary event. This finding is in good agreement with the increased retrograde transport rate of lysosomes in the axon of primary MNs *ex vivo*, presumably ultimately leading to a buildup of lysosomes at the distal end of the AIS, but a reduced delivery of the axonal tracer to the soma observed *in vivo*. The decreased delivery of FG to the soma at later time points seems contradictory, given a higher transport of FG-containing organelles. However, it seems reasonable that the tracer gets stuck in the vacuoles (of which the majority are FG positive), finally leading to impaired somatic delivery. Surprisingly, the observed severe vacuolization of the FMN has only small functional consequences, reflected by very mild behavioral deficits. At 2 months of age, NMJs remain intact despite clear vacuolization. Furthermore, vacuolization seems not to completely impair axonal trafficking, allowing survival of the proximal axon, the NMJ, and finally the MN itself. However, denervation of NMJs in aged animals indicates a functional decline. Notably, the AIS pathology might additionally explain the observed functional behavioral and motoric alterations despite a lack of degeneration in young animals: alterations of the AIS due to, for example, mutations in Tau were shown to affect neuronal excitability (Sohn et al., 2019). Similarly, the altered morphology of the AIS in *Tmem106b* KO mice might cause functional deficits.

It is tempting to speculate that lysosomes or retrogradely transported late endosomes accumulating within or at the distal end of the AIS undergo aberrant fusion, ultimately leading to the ballooning of the axon. These lysosomes are likely dysfunctional and unable to degrade any cargo, which might explain the slight increase in some lysosomal enzymes and soluble proteins like CatD or progranulin, considering that (active) lysosomal

proteases regulate the levels of lysosomal enzymes. This explanation is additionally supported by the unchanged transcript levels of the investigated enzymes, suggesting posttranscriptional regulation of the levels of these enzymes or modulation of their activity. We can also not rule out that TMEM106B is directly modulating their function, explaining the increased activity, and that in fact, the giant vacuoles are a consequence of such a dysregulation. The increase of progranulin is particularly interesting, given the close genetic interaction between *GRN* and *TMEM106B* in human FTLD patients. However, given an increase of other lysosomal proteins to a similar extent, we think this finding is not specific for progranulin but rather reflects the general lysosomal alterations. Nevertheless, we cannot fully rule out the possibility that TMEM106B directly affects progranulin levels by a direct physical interaction (e.g., protecting progranulin from proteolysis).

Alternatively to the suggested aberrant fusion hypothesis, TMEM106B could have a dual function, involving the cytosolic N terminus mediating the retrograde microtubule-dependent transport of lysosomes by interacting directly or indirectly with motor proteins and the luminal domain mediating fusion events and/or activity of lysosomal enzymes. This might also explain alterations in autophagy, which could lead both to defects in fusion and to indirect effects due to impaired lysosomal degradation. Of note, our study provides experimental evidence for a sorting mechanism for LAMP1-positive organelles at the distal end of the AIS and suggests the presence of "gatekeeper" machinery facilitating the retrograde entry of lysosomes into the AIS. Other mechanisms are also conceivable: the entry of axonal retrograde cargo into the AIS might be limiting, and through TMEM106B deficiency, too much cargo is transported to the AIS, exceeding its capacity. Microtubule modifications or motor preference might differ between the distal end of the AIS and the proximal axon and cause the disassembly of the motor and LAMP1-positive cargo. Finally, the AIS is the site where myelin sheath begins, and myelination might be critical for the formation of the vacuoles. The precise mechanism by which vacuoles develop *in situ* at the distal end of the AIS remains to be determined. Previous studies reported that the fusion between LAMP1-positive endosomes and autophagosomes in axons is an early event, taking place in the distal axon. During retrograde transport, these organelles mature, but the final maturation and acidification take place as a last step in the soma (Maday et al., 2014). It is also possible to hypothesize that the AIS is critical during this process, sorting retrograde transported autophagosomes/amphisomes to the soma for their final maturation.

An interesting observation is the very restricted occurrence of the vacuoles in selected MN nuclei. MNs show an extreme degree of polarization and are characterized by exceedingly long axons and highly complex arborization, making them susceptible to any (even subtle) alterations in the axonal transport of organelles. TMEM106B is expressed ubiquitously in neurons, and there is no pronounced higher expression in MNs compared to other neuronal subpopulations. Though we cannot finally prove this hypothesis, we speculate that the complexity in the axonal arborization and the long distances that need to be overcome by LAMP1-positive organelles in axons of MNs might explain their predominant susceptibility.

The "protective" effect of *TMEM106B* coding variants in humans with FTLD has been suggested to be the result of reduced expression due to decreased stability of the resulting protein bearing the T185S amino acid exchange (Nicholson et al., 2013; Van Deerlin et al., 2010). The situation in the KO with a full deletion instead of possibly slightly reduced protein levels due to the T185S variant is, however, clearly different and likely has a much higher impact on cellular function and resulting dysfunction. It should be noted that the purpose of our present study was not to generate a model for FTLD, but to get a better understanding of the physiological function of TMEM106B. Variants in *TMEM106B* were initially found to convey the highest effect on *GRN* carriers, but later studies revealed a significant effect on *C9orf72* carriers as well, implying that TMEM106B acts *in trans* to both *GRN* and *C9orf72* mutations. Our proposed model of impaired lysosomal degradation based on altered axonal trafficking leads us to the hypothesis that mutations in progranulin and perhaps C9orf72 affect lysosomal proteolysis and that alterations in TMEM106B additionally titrate disease risk and severity in a dose-dependent manner. Moreover, the observed accumulation of lipofuscin in the *Tmem106b* KO mice, presumably caused by axonal transport defects, might explain the effect of genetic *TMEM106B* variations on aging and cognition (Rhinn and Abeliovich, 2017; White et al., 2017), considering that an age-dependent lysosomal lipofuscin accumulation is one of the hallmarks of neuronal aging.

STAR★METHODS

Detailed methods are provided in the online version of this paper and include the following:

- KEY RESOURCES TABLE
- LEAD CONTACT AND MATERIALS AVAILABILITY
- EXPERIMENTAL MODEL AND SUBJECT DETAILS
  - Animal Models
  - Primary Cells
- METHOD DETAILS
  - Quantitative real time PCR (qRT-PCR)
  - Biochemical Experiments
  - Histology and electron microscopy
- *IN VIVO* LABELING WITH FLUORO-GOLD RETROGRADE TRACER
  - Behavioral Studies
  - Immunocytochemistry and live-cell imaging
  - Immunocytochemistry
- QUANTIFICATION AND STATISTICAL ANALYSIS
- DATA AND CODE AVAILABILITY

SUPPLEMENTAL INFORMATION

Supplemental Information can be found online at https://doi.org/10.1016/j.celrep.2020.02.060.

ACKNOWLEDGMENTS

We thank Dagmar Niemeier, Maike Langer, and Katrin Fellerer for excellent technical assistance and Björn Schuster, Inken Beck, and Radislav Sedlacek (Institute of Molecular Genetics, Prague) for the generation of *Tmem106b*

CRISPR KO mice. M.D. and P.S. are supported by the Deutsche Forschungsgemeinschaft (DFG) FOR2625. B.K. is supported by the DFG through SFB 1149. C.H. is supported by the DFG within the framework of the Munich Cluster for Systems Neurology (EXC 1010 SyNergy, ID 390857198) and a DFG-funded Koselleck Project (HA1737/16-1). W.W. is supported by the DFG through SFB 870 and by the "EUCOMM: Tools for Functional Annotation of the Mouse Genome" (EUCOMMTOOLS) project (FP7-HEALTH-F4-2010-261492).

AUTHOR CONTRIBUTIONS

P.L., G.W., S.S., S.K., B.D., D.S., R.W., R.L-R., and M.D. performed experimental work. P.L., G.W., S.S., B.W., W.W., R.D.H., Y.U., M.S., C.H., P.S., B.K., A.C., and M.D. were involved in experimental design and data analysis and interpretation, and they also edited the manuscript. M.D. conceived the study and wrote the manuscript.

DECLARATION OF INTERESTS

The authors declare no competing interests.

Received: February 14, 2019
Revised: October 21, 2019
Accepted: February 13, 2020
Published: March 10, 2020

REFERENCES

Arrant, A.E., Nicholson, A.M., Zhou, X., Rademakers, R., and Roberson, E.D. (2018). Partial Tmem106b reduction does not correct abnormalities due to progranulin haploinsufficiency. Mol. Neurodegener. *13*, 32.

Baker, M., Mackenzie, I.R., Pickering-Brown, S.M., Gass, J., Rademakers, R., Lindholm, C., Snowden, J., Adamson, J., Sadovnick, A.D., Rollinson, S., et al. (2006). Mutations in progranulin cause tau-negative frontotemporal dementia linked to chromosome 17. Nature *442*, 916–919.

Brady, O.A., Zheng, Y., Murphy, K., Huang, M., and Hu, F. (2013). The frontotemporal lobar degeneration risk factor, TMEM106B, regulates lysosomal morphology and function. Hum. Mol. Genet. *22*, 685–695.

Busch, J.I., Unger, T.L., Jain, N., Tyler Skrinak, R., Charan, R.A., and Chen-Plotkin, A.S. (2016). Increased expression of the frontotemporal dementia risk factor TMEM106B causes C9orf72-dependent alterations in lysosomes. Hum. Mol. Genet. *25*, 2681–2697.

Chen-Plotkin, A.S., Unger, T.L., Gallagher, M.D., Bill, E., Kwong, L.K., Volpicelli-Daley, L., Busch, J.I., Akle, S., Grossman, M., Van Deerlin, V., et al. (2012). TMEM106B, the risk gene for frontotemporal dementia, is regulated by the microRNA-132/212 cluster and affects progranulin pathways. J. Neurosci. *32*, 11213–11227.

Cheng, X.T., Xie, Y.X., Zhou, B., Huang, N., Farfel-Becker, T., and Sheng, Z.H. (2018). Characterization of LAMP1-labeled nondegradative lysosomal and endocytic compartments in neurons. J. Cell Biol. *217*, 3127–3139.

Claussen, M., Kübler, B., Wendland, M., Neifer, K., Schmidt, B., Zapf, J., and Braulke, T. (1997). Proteolysis of insulin-like growth factors (IGF) and IGF binding proteins by cathepsin D. Endocrinology *138*, 3797–3803.

Clayton, E.L., Milioto, C., Muralidharan, B., Norona, F.E., Edgar, J.R., Soriano, A., Jafar-Nejad, P., Rigo, F., Collinge, J., and Isaacs, A.M. (2018). Frontotemporal dementia causative CHMP2B impairs neuronal endolysosomal trafficrescue by TMEM106B knockdown. Brain *141*, 3428–3442.

Crawley, J.N. (2007). What's Wrong With My Mouse?: Behavioral Phenotyping of Transgenic and Knockout Mice, Second Edition (Wiley).

Cruts, M., Gijselinck, I., van der Zee, J., Engelborghs, S., Wils, H., Pirici, D., Rademakers, R., Vandenberghe, R., Dermaut, B., Martin, J.J., et al. (2006). Null mutations in progranulin cause ubiquitin-positive frontotemporal dementia linked to chromosome 17q21. Nature *442*, 920–924.

Dombert, B., Sivadasan, R., Simon, C.M., Jablonka, S., and Sendtner, M. (2014). Presynaptic localization of Smn and hnRNP R in axon terminals of embryonic and postnatal mouse motoneurons. PLoS ONE *9*, e110846.

Finch, N., Carrasquillo, M.M., Baker, M., Rutherford, N.J., Coppola, G., Dejesus-Hernandez, M., Crook, R., Hunter, T., Ghidoni, R., Benussi, L., et al. (2011). TMEM106B regulates progranulin levels and the penetrance of FTLD in GRN mutation carriers. Neurology *76*, 467–474.

Gallagher, M.D., Suh, E., Grossman, M., Elman, L., McCluskey, L., Van Swieten, J.C., Al-Sarraj, S., Neumann, M., Gelpi, E., Ghetti, B., et al. (2014). TMEM106B is a genetic modifier of frontotemporal lobar degeneration with C9orf72 hexanucleotide repeat expansions. Acta Neuropathol. *127*, 407–418.

Gallagher, M.D., Posavi, M., Huang, P., Unger, T.L., Berlyand, Y., Gruenewald, A.L., Chesi, A., Manduchi, E., Wells, A.D., Grant, S.F.A., et al. (2017). A Dementia-Associated Risk Variant near TMEM106B Alters Chromatin Architecture and Gene Expression. Am. J. Hum. Genet. *101*, 643–663.

Gass, J., Cannon, A., Mackenzie, I.R., Boeve, B., Baker, M., Adamson, J., Crook, R., Melquist, S., Kuntz, K., Petersen, R., et al. (2006). Mutations in progranulin are a major cause of ubiquitin-positive frontotemporal lobar degeneration. Hum. Mol. Genet. *15*, 2988–3001.

Gey, M., Wanner, R., Schilling, C., Pedro, M.T., Sinske, D., and Knöll, B. (2016). Atf3 mutant mice show reduced axon regeneration and impaired regeneration-associated gene induction after peripheral nerve injury. Open Biol. *6*, 160091.

Ghazi-Noori, S., Froud, K.E., Mizielinska, S., Powell, C., Smidak, M., Fernandez de Marco, M., O'Malley, C., Farmer, M., Parkinson, N., Fisher, E.M., et al. (2012). Progressive neuronal inclusion formation and axonal degeneration in CHMP2B mutant transgenic mice. Brain *135*, 819–832.

Götzl, J.K., Mori, K., Damme, M., Fellerer, K., Tahirovic, S., Kleinberger, G., Janssens, J., van der Zee, J., Lang, C.M., Kremmer, E., et al. (2014). Common pathobiochemical hallmarks of progranulin-associated frontotemporal lobar degeneration and neuronal ceroid lipofuscinosis. Acta Neuropathol. *127*, 845–860.

Gutzmann, A., Ergül, N., Grossmann, R., Schultz, C., Wahle, P., and Engelhardt, M. (2014). A period of structural plasticity at the axon initial segment in developing visual cortex. Front. Neuroanat. *8*, 11.

Klein, Z.A., Takahashi, H., Ma, M., Stagi, M., Zhou, M., Lam, T.T., and Strittmatter, S.M. (2017). Loss of TMEM106B Ameliorates Lysosomal and Frontotemporal Dementia-Related Phenotypes in Progranulin-Deficient Mice. Neuron *95*, 281–296.e286.

Lang, C.M., Fellerer, K., Schwenk, B.M., Kuhn, P.H., Kremmer, E., Edbauer, D., Capell, A., and Haass, C. (2012). Membrane orientation and subcellular localization of transmembrane protein 106B (TMEM106B), a major risk factor for frontotemporal lobar degeneration. J. Biol. Chem. *287*, 19355–19365.

Lüningschrör, P., Binotti, B., Dombert, B., Heimann, P., Perez-Lara, A., Slotta, C., Thau-Habermann, N., R von Collenberg, C., Karl, F., Damme, M., et al. (2017). Plekhg5-regulated autophagy of synaptic vesicles reveals a pathogenic mechanism in motoneuron disease. Nat. Commun. *8*, 678.

Maday, S., Twelvetrees, A.E., Moughamian, A.J., and Holzbaur, E.L. (2014). Axonal transport: cargo-specific mechanisms of motility and regulation. Neuron *84*, 292–309.

Markmann, S., Krambeck, S., Hughes, C.J., Mirzaian, M., Aerts, J.M., Saftig, P., Schweizer, M., Vissers, J.P., Braulke, T., and Damme, M. (2017). Quantitative Proteome Analysis of Mouse Liver Lysosomes Provides Evidence for Mannose 6-phosphate-independent Targeting Mechanisms of Acid Hydrolases in Mucolipidosis II. Mol. Cell. Proteomics *16*, 438–450.

Mitchell, K.J., Pinson, K.I., Kelly, O.G., Brennan, J., Zupicich, J., Scherz, P., Leighton, P.A., Goodrich, L.V., Lu, X., Avery, B.J., et al. (2001). Functional analysis of secreted and transmembrane proteins critical to mouse development. Nat. Genet. *28*, 241–249.

Nelson, P.T., Dickson, D.W., Trojanowski, J.Q., Jack, C.R., Boyle, P.A., Arfanakis, K., Rademakers, R., Alafuzoff, I., Attems, J., Brayne, C., et al. (2019). Limbic-predominant age-related TDP-43 encephalopathy (LATE): consensus working group report. Brain *142*, 1503–1527.

Nicholson, A.M., Finch, N.A., Wojtas, A., Baker, M.C., Perkerson, R.B., 3rd, Castanedes-Casey, M., Rousseau, L., Benussi, L., Binetti, G., Ghidoni, R., et al. (2013). TMEM106B p.T185S regulates TMEM106B protein levels: implications for frontotemporal dementia. J. Neurochem. *126*, 781–791.

Nicholson, A.M., Zhou, X., Perkerson, R.B., Parsons, T.M., Chew, J., Brooks, M., DeJesus-Hernandez, M., Finch, N.A., Matchett, B.J., Kurti, A., et al. (2018). Loss of Tmem106b is unable to ameliorate frontotemporal dementia-like phenotypes in an AAV mouse model of C9ORF72-repeat induced toxicity. Acta Neuropathol. Commun. *6*, 42.

Pottier, C., Zhou, X., Perkerson, R.B., III, Baker, M., Jenkins, G.D., Serie, D.J., Ghidoni, R., Benussi, L., Binetti, G., López de Munain, A., et al. (2018). Potential genetic modifiers of disease risk and age at onset in patients with frontotemporal lobar degeneration and GRN mutations: a genome-wide association study. Lancet Neurol. *17*, 548–558.

Premi, E., Grassi, M., van Swieten, J., Galimberti, D., Graff, C., Masellis, M., Tartaglia, C., Tagliavini, F., Rowe, J.B., Laforce, R., Jr., et al.; Genetic FTD Initiative (GENFI) (2017). Cognitive reserve and TMEM106B genotype modulate brain damage in presymptomatic frontotemporal dementia: a GENFI study. Brain *140*, 1784–1791.

Ratnavalli, E., Brayne, C., Dawson, K., and Hodges, J.R. (2002). The prevalence of frontotemporal dementia. Neurology *58*, 1615–1621.

Rhinn, H., and Abeliovich, A. (2017). Differential Aging Analysis in Human Cerebral Cortex Identifies Variants in TMEM106B and GRN that Regulate Aging Phenotypes. Cell Syst *4*, 404–415.e405.

Schmued, L.C., and Fallon, J.H. (1986). Fluoro-Gold: a new fluorescent retrograde axonal tracer with numerous unique properties. Brain Res. *377*, 147–154.

Schwenk, B.M., Lang, C.M., Hogl, S., Tahirovic, S., Orozco, D., Rentzsch, K., Lichtenthaler, S.F., Hoogenraad, C.C., Capell, A., Haass, C., and Edbauer, D. (2014). The FTLD risk factor TMEM106B and MAP6 control dendritic trafficking of lysosomes. EMBO J. *33*, 450–467.

Shi, Y., Lin, S., Staats, K.A., Li, Y., Chang, W.H., Hung, S.T., Hendricks, E., Linares, G.R., Wang, Y., Son, E.Y., et al. (2018). Haploinsufficiency leads to neurodegeneration in C9ORF72 ALS/FTD human induced motor neurons. Nat. Med. *24*, 313–325.

Shibata, M., Kanamori, S., Isahara, K., Ohsawa, Y., Konishi, A., Kametaka, S., Watanabe, T., Ebisu, S., Ishido, K., Kominami, E., and Uchiyama, Y. (1998). Participation of cathepsins B and D in apoptosis of PC12 cells following serum deprivation. Biochem. Biophys. Res. Commun. *251*, 199–203.

Sohn, P.D., Huang, C.T., Yan, R., Fan, L., Tracy, T.E., Camargo, C.M., Montgomery, K.M., Arhar, T., Mok, S.A., Freilich, R., et al. (2019). Pathogenic Tau Impairs Axon Initial Segment Plasticity and Excitability Homeostasis. Neuron *104*, 458–470.e5.

Stagi, M., Klein, Z.A., Gould, T.J., Bewersdorf, J., and Strittmatter, S.M. (2014). Lysosome size, motility and stress response regulated by fronto-temporal dementia modifier TMEM106B. Mol. Cell. Neurosci. *61*, 226–240.

Tropea, T.F., Mak, J., Guo, M.H., Xie, S.X., Suh, E., Rick, J., Siderowf, A., Weintraub, D., Grossman, M., Irwin, D., et al. (2019). TMEM106B Effect on cognition in Parkinson disease and frontotemporal dementia. Ann. Neurol. *85*, 801–811.

van Blitterswijk, M., Mullen, B., Nicholson, A.M., Bieniek, K.F., Heckman, M.G., Baker, M.C., DeJesus-Hernandez, M., Finch, N.A., Brown, P.H., Murray, M.E., et al. (2014). TMEM106B protects C9ORF72 expansion carriers against frontotemporal dementia. Acta Neuropathol. *127*, 397–406.

Van Deerlin, V.M., Sleiman, P.M., Martinez-Lage, M., Chen-Plotkin, A., Wang, L.S., Graff-Radford, N.R., Dickson, D.W., Rademakers, R., Boeve, B.F., Grossman, M., et al. (2010). Common variants at 7p21 are associated with frontotemporal lobar degeneration with TDP-43 inclusions. Nat. Genet. *42*, 234–239.

van der Zee, J., Van Langenhove, T., Kleinberger, G., Sleegers, K., Engelborghs, S., Vandenberghe, R., Santens, P., Van den Broeck, M., Joris, G., Brys, J., et al. (2011). TMEM106B is associated with frontotemporal lobar degeneration in a clinically diagnosed patient cohort. Brain *134*, 808–815.

Wanner, R., Gey, M., Abaei, A., Warnecke, D., de Roy, L., Dürselen, L., Rasche, V., and Knöll, B. (2017). Functional and Molecular Characterization of a Novel Traumatic Peripheral Nerve-Muscle Injury Model. Neuromolecular Med. *19*, 357–374.

White, C.C., Yang, H.S., Yu, L., Chibnik, L.B., Dawe, R.J., Yang, J., Klein, H.U., Felsky, D., Ramos-Miguel, A., Arfanakis, K., et al. (2017). Identification of genes associated with dissociation of cognitive performance and neuropathological burden: Multistep analysis of genetic, epigenetic, and transcriptional data. PLoS Med. *14*, e1002287.

Yau, K.W., Schätzle, P., Tortosa, E., Pagès, S., Holtmaat, A., Kapitein, L.C., and Hoogenraad, C.C. (2016). Dendrites In Vitro and In Vivo Contain Microtubules of Opposite Polarity and Axon Formation Correlates with Uniform Plus-End-Out Microtubule Orientation. J. Neurosci. *36*, 1071–1085.

STAR★METHODS

KEY RESOURCES TABLE

REAGENT or RESOURCE	SOURCE	IDENTIFIER
Antibodies		
Rabbit-polyclonal TMEM106B	Bethyl Antibodies	Cat# A303-439A, RRID:AB_10953337
Rat-monoclonal TMEM106B Clone 6F2	Lang et al., 2012	Clone 6F2
Rabbit polyclonal p62	MBL	Cat# PM045, RRID:AB_1279301
Rabbit-polyclonal Calnexin	Stressgen / Enzo	Cat# ADI-SPA-860, RRID:AB_10616095
Goat-polyclonal Cathepsin D C-20	Santa Cruz Biotechnology	Cat# sc-6486, RRID:AB_637896
Rabbit polyclonal cathepsin D	Shibata et al., 1998	N/A
Rabbit-monoclonal GRN Clone 8H10	Götzl et al., 2014	N/A
Mouse-monoclonal Ubiqutin (clone P4D1)	Santa Cruz Biotechnology	Cat# sc-8017, RRID:AB_628423
Rabbit-polyclonal LC3B	Novus	Cat# NB100-2220, RRID:AB_10003146
Mouse-monoclonal beta-Actin Clone AC-74	Sigma-Aldrich	Cat# A2228, RRID:AB_476697
Goat polyclonal Ankyrin G (P-20)	Santa Cruz Biotechnology	Cat# sc-31778, RRID:AB_2289736
Rabbit-polyclonal βIV-spectrin	Gutzmann et al., 2014	N/A
Rabbit-polyclonal FluoroGold	Millipore	Cat# AB153 RRID:AB_90738
Rat-monoclonal LAMP-1 Clone 1D4B	DSHB	RRID:AB_2134500
Mouse-monoclonal neurofilament (NF-M) Clone 2H3	DSHB	RRID:AB_531793
Rabbit-polyclonal Myelin basic protein antibody (MBP)	GeneTex	Cat# GTX22404, RRID:AB_370733
Mouse-monoclonal Tuj1	Neuromics	Cat# MO15013, RRID:AB_2737114
Mouse-monoclonal NeuN	Millipore	Cat# mAbA60, RRID:AB_2314891
Rabbit-polyclonal Iba1	GeneTex	Cat# GTX100042, RRID:AB_1240434
Rabbit-polyclonal COX IV	Abcam	Cat# ab16056, RRID:AB_443304
Rabbit-polyclonal ChAT	Synaptic Systems	Cat# 297 013, RRID:AB_2620040)
Rabbit-polyclonal Anti-Fluorescent Gold Antibody	Millipore	Cat# AB153-I, RRID:AB_2632408)
Goat anti-rabbit IgG Alexa Fluor 488	Invitrogen	RRID: AB_143165
Goat anti-rat IgG Alexa Fluor 594	Invitrogen	RRID: AB_10561522
Goat anti-rabbit IgG Alexa Fluor 647	Invitrogen	RRID: AB_2535812
Goat anti-rabbit IgG Alexa Fluor 488	Invitrogen	RRID: AB_143165
Goat anti-rat IgG Alexa Fluor 594	Invitrogen	RRID: AB_10561522
Goat anti-rabbit IgG Alexa Fluor 647	Invitrogen	RRID: AB_2535813
Donkey anti-sheep Alexa Fluor 594	Invitrogen	RRID: AB_2534083
Biological Samples		
ES Cell clone: Clone EPD0047_1_E02	KOMP consortium	RRID:MMRRC_050092-UCD
Chemicals, Peptides, and Recombinant Proteins		
FluoroGold	Fluorochrome	https://fluorochrome.com/flouro-gold/
α-Bungarotoxin, Alexa Fluor 488 conjugate	Invitrogen	Cat# B13422
LysoTracker Red DND-99	Invitrogen	Cat# L7528
Experimental Models: Organisms/Strains		
Mouse line: *Tmem106b*^{del2bp}	This paper	N/A
Mouse line: *Tmem106b*^{tm2a}	This paper	N/A
Oligonucleotides		
Tmem106b_ex3_F: GGTTTCCTTGTATCAGACATTAC	Sigma-Aldrich	N/A
Tmem106b_ex3_R: GCTTAACTCACTTCTATTACTGC	Sigma-Aldrich	N/A
Tmem106b_CE_F: GGCGTTACATCGACAGACAA	Sigma-Aldrich	N/A
Tmem106b_CE_R: TGAGAGACATCTCCATTTCTTCC	Sigma-Aldrich	N/A

(*Continued on next page*)

Continued

REAGENT or RESOURCE	SOURCE	IDENTIFIER
For1: TTCTCTCCATGTGCTGCATTATGAGC	Sigma-Aldrich	N/A
Rev1: ACGTGCTTCTCTCATCTACAGTTTTCC	Sigma-Aldrich	N/A
For2: GGGATCTCATGCTGGAGTTCTTCG	Sigma-Aldrich	N/A
Rev2: GAGATGGCGCAACGCAATTAATG	Sigma-Aldrich	N/A
Tmem106b: 5′-GCTGCTGCTAGCACCATGGGAAA GTCTCTTTCTCACTTACC-3′	Metabion	N/A
Tmem106b: 5′-GCTGCTACCGGTTTGTTGTGGCTGA AGGACATTTAG-3′	Metabion	N/A
mCherry: 5′- GCTGCTACCGGTGGAGGTGGT GGA TCTTCTGTGAGCAAGGGCGAGGAGGATAACATGG–3′	Metabion	N/A
mCherry: 5′-GCTGCTTCTAGATTACTTGTACAGCTCGTCC –3′	Metabion	N/A
Recombinant DNA		
FUW-Tmem106b-mCherry	this study	N/A
LAMP1-mGFP	Addgene	#21075
pmRFP-LC3	Addgene	#34831
FUW-RFP-GFP-LC3	Lüningschrör et al., 2017	PMID: 29084947
FUW-RFP-LC3	this study	N/A
FUW -Lamp1-mGFP	this study	N/A
FUW-RFP-LC3-CMV::Lamp1-mGFP	this study	N/A
Software and Algorithms		
GraphPad Prism	GraphPad	RRID:SCR_002798
Templo Software	CONTEMPLAS GmbH	N/A
Vicon Motus 2D software	CONTEMPLAS GmbH	N/A

LEAD CONTACT AND MATERIALS AVAILABILITY

Plasmids, not covered by any restrictions like MTAs generated in this study are available upon request. Further information and requests for resources and reagents should be directed to and will be fulfilled by the Lead Contact, Markus Damme (mdamme@biochem.uni-kiel.de).

EXPERIMENTAL MODEL AND SUBJECT DETAILS

Animal Models

Generation of Tmem106b knockout Mice by CRISPR/Cas9

For the generation of *Tmem106b* KO mice by CRISPR/Cas9-mediated targeting of the *Tmem106b* locus, a guide RNA (gRNA_Tmem106b F1; sequence: AGTGAAGTGCACAACGAAGACGG; protospacer adjacent motif (PAM) is underlined) was designed, that targets exon 3, the first coding exon in the *Tmem106b* gene. The gRNA overlaps with a BbsI restriction site. Single-cell embryos from C57BL/6 mice were co-injected with Cas9 mRNA and gRNA_Tmem106b F1 gRNA. The resulting mutations after non-homologous end-joining repair identified after screening of the offspring in founder mouse lines were validated by Sanger-sequencing. The two chosen founder lines contained either a 2bp deletion (#30907) or a 1bp insertion (#29772); both leading to frameshift mutations. Founder mice were mated with C57BL/6 and germline transmission of the mutation was validated again by Sanger sequencing. A founder line with a 2bp deletion was selected for further experiments, but another strain with a 1bp insertion was phenotypically indistinguishable. The following generations of mice were routinely genotyped by PCR with genomic tail DNA as a template followed by restriction enzyme digest with BbsI and agarose gel electrophoresis or capillary electrophoresis. Primers for amplification of a 552bp fragment of the wild-type locus partially covering exon 3 are: Tmem106b_ex3_F: GGTTTCCTTGTATCAGACATTAC; Tmem106b_ex3_R: GCTTAACTCACTTCTATTACTGC. Alternatively, PCR products amplifying a smaller fragment (121bp of the wild-type locus partially covering exon 3, sequences: Tmem106b_CE_F: GGCGTTACATCGACAGACAA; Tmem106b_CE_R: TGAGAGACATCTCCATTTCTTCC) were separated by capillary electrophoresis with a QIAXcel electrophoresis device (QIAGEN).

Generation of Tmem106b *KO mice with targeted embryonic stem (ES) cells*

Targeted ES cells were obtained from the KOMP consortium (Clone EPD0047_1_E02) and provided by the MMRRC consortium. Generation, breeding and analysis of mice were in line with local and national guidelines and has been approved by the local authorities. ES cells were injected into BALB/C blastocysts. The obtained chimeric mice were bred C57BL/6N wild-type mice to

obtain germline transmission. In the resulting mouse line (tm2a, Knockout-first), expression of *Tmem106b* is disrupted by a splice acceptor (SA) site in the intronic sequence between exons 3 and 4. A β-galactosidase reporter gene (lacZ) is expressed under the control of the endogenous *Tmem106b* promoter. Mice carrying the tm2a allele were bred with Cre-deleter mice which constitutively express the recombinase under the control of the Gt(ROSA)26Sor gene. Mice were genotyped with PCRs for the wild-type-allele, covering a 301 bp sequence in the intronic sequence between exon 3 and exon 4 (For1: TTCTCTCCATGTGCTGCATTATGAGC and Rev1: ACGTGCTTCTCTCATCTACAGTTTTCC) and the tm2b allele, covering partially the targeting cassette and the intronic sequence between exon 4 and exon 5 (For2: GGGATCTCATGCTGGAGTTCTTCG and Rev2: GAGATGGCGCAACGCAATTAATG). Animals for all phenotypic analyses were generated by heterozygous mating of mice with the *Tmem106b* tm2b allele.

Mice were housed at standard laboratory conditions (12 hours light/dark cycle, constant room temperature and humidity). Behavioral testing took place during the light phase of the cycle. Food and water were available *ad libitum*. Experimental protocols were approved by the ethical research committee of the KU Leuven according to EC guidelines or were approved by local german authorities (Ministerium für Energiewende, Landwirtschaft, Umwelt, Natur und Digitalisierung; AZ V242-4255/2018; Regierungspräsidium Tübingen, Germany; TVA 1368). Mice of both genders were used for histology and biochemistry experiments. For the behavioral studies, only female mice were used. The age of the animals is indicated for every experiment, generally animals between two and six months were used, with the exception of the eye blink and whisker orienting reflex tests and balance beam test, in which 14 months old animals were inlcuded.

Primary Cells

Primary MN culture

Murine embryonic spinal MNs were isolated and cultured as described (Lüningschrör et al., 2017). Briefly, after dissection of the ventrolateral part of E12.5 embryos, spinal cord tissues were incubated for 15 minutes in 0.1% trypsin in Hank's balanced salt solution. Cells were triturated and incubated in Neurobasal medium (Invitrogen, CA, USA), supplemented with 1 × Glutamax (Invitrogen, CA, USA) on Nunclon plates (Nunc) pre-coated with antibodies against the p75 NGF receptor (MLR2, kind gift of Robert Rush, Flinders University, Adelaide, Australia) for 45 minutes. Plates were washed three times with Neurobasal medium, and the remaining MN were recovered from the plate with depolarization solution (0.8% NaCl, 35 mM KCl and 2 mM $CaCl_2$) and collected in MN medium (2% horse serum, 1x B27 in Neurobasal medium with 1x Glutamax).

METHOD DETAILS

Quantitative real time PCR (qRT-PCR)

Total RNA was prepared from homogenized mouse brain using the QIAshredder and RNeasy Mini Kit (QIAGEN) according to manufacturer's instructions. 2 μg of RNA was reverse transcribed into cDNA using SuperScript IV reverse transcriptase (Thermo Fisher Scientific Termofisher) and random hexamer primers (Promega). The following primer sets from Integrated DNA Technologies were used: mouse Ctsd Mm.PT.53a.7639164 (Exon boundary 4 to 5), mouse Glb1 Mm.PT.58.8893651 (Exon boundary 4 to 6), Gusb Mm.PT.39a.22214848 (Exon boundary 1 to 2), Hexb Mm.PT.58.6976437 (Exon boundary 6 to 7) and Man2b1 Mm.PT.58.11143577 (Exon boundary 16 to 17). cDNA levels were measured in triplicates using TaqMan assays on a 7500 Fast Real-Time-PCR System (Applied Biosystems), normalized to Hrtp1 Mm.PT.39a.22214828. cDNA expression and relative transcription levels of the respective sequences were analyzed using the comparative delta Ct method (7500 Software V2.0.5, Applied Biosystems, Life Technologies).

Biochemical Experiments

Brain extracts and immunoblotting

Snap frozen brain tissue was mechanically powdered in liquid nitrogen and lysed in RIPA buffer (150 mM NaCl, 20 mM Tris–HCl pH 7.4, 1% NP40, 0.05% Triton X-100, 0.5% sodium-desoxycholate, 2.5 mM ETDA) using the Precellys lysing kit (Ref.: P00933-LYSK0-A) followed by centrifugation at 17,000 × g, 4°C for 45 minutes. Supernatants were collected and protein concentration was determined using BC assay. For SDS-PAGE samples were boiled in Laemmli sample buffer and separated on TRIS-glycine gels. Proteins were transferred onto polyvinylidene difluoride membranes (GE Healthcare Life Science; Amersham Hybond PVDF,) or nitrocellulose membranes (GE Healthcare Life Science). Membranes were blocked for one hour in I-Block™ (Thermo Fisher Scientific) and exposed to the indicated antibody. HRP-conjugated antibodies and Pierce ECL Plus Western Blotting Substrate (Thermo Fisher Scientific) were used for detection and visualization. The following antibodies were used: Cathepsin D (Santa Cruz, sc-6486), GRN (clone 8H10) (Götzl et al., 2014), TMEM106B (A303-439A, Bethyl Antibodies) (Götzl et al., 2014), TMEM106B (clone 6F2) (Lang et al., 2012), calnexin (Stressgen, SPA-860), ubiquitin (Santa Cruz; clone P4D1), p62 (MBL, PM045), LC3 (Novus Biologicals, NB100-2220), actin (Sigma-Aldrich).

Enzymatic assays for lysosomal hydrolases

Brain tissue was homogenized with a potter Elvehjem in 15 volumes (w/v) ice-cold TBS containing 0.5% Triton X-100 and protease inhibitor cocktail. After incubation on ice for 30 minutes with vortexing, lysates were cleared by centrifugation. The specific activity of lysosomal hydrolases was determined as described previously (Markmann et al., 2017) with the following 4-Nitrophenyl-conjugated

substrates (all 10 mM): p-Nitrophenyl-α-D-mannopyranoside (α-mannosidase), p-Nitrophenyl-β-D-glucuronide (β-glucuronidase), p-Nitrophenyl-β-D-glucopyranoside (β-hexosaminidase), p-Nitrophenyl-β-D-galactopyranoside (β-galactosidase).

Histology and electron microscopy

Immunofluorescence of brain and nerve tissues

Mice were deeply anaesthetized and perfused through the left heart ventricle with 0.1 M phosphate buffer (PB) (pH 7.4) followed by perfusion with 4% paraformaldehyde (PFA) in PB. After tissue removal, tissues were post-fixed for another 4 hours in 4% PFA and subsequently transferred to 30% sucrose (in PB) over night. 35 μm thick free-floating sections were cut with a sliding microtome (SM2000R, Leica). For antibody-labeling, sections were washed in PB, blocked with 4% normal goat serum and 0.5% Triton X-100 in 0.1 M PB for one hour at room temperature (RT) and subsequently incubated with the primary antibodies at 4°C over night in blocking solution. After washing three times with PB containing 0.25% Triton X-100, sections were incubated with AlexaFluor fluorophore-conjugated secondary antibodies (AlexaFluor 488, 594 or 647) (Life Technologies) for one hour at RT and washed again three times with PB containing 0.25% Triton X-100. Finally, sections were mounted in Mowiol/DABCO containing DAPI. Images were taken with an Olympus confocal microscope (FV1000, Olympus). STED images were acquired with a Stedycon STED (Abberior Instruments) microscope. The following antibodies were used: AnkyrinG (Santa Cruz, P-20), βIV-spectrin (kind gift from Maren Engelhardt, Gutzmann et al., 2014), LAMP1 (DSHB, Hybridoma Bank, clone 1D4B), cathepsin D (gift from Thomas Braulke, Claussen et al., 1997), Neurofilament H (DSHB, Hybridoma Bank, clone 2H3) Myelin Basic Protein (MBP) (Genetex, GTX22404), NeuN (Millipore, clone A60), Iba1 (Genetex, GTX100042), Cox IV (Abcam, ab16056), ChAT (#297 013, Synaptic Systems), FluoroGold™ (AB153, Millipore).

X-gal staining for β-galactosidase reporter gene expression analysis

For β-galactosidase reporter gene expression analysis, free floating sections from heterozygote tm2b-mice were permeabilized for 10 minutes in PBS containing 0.01% (w/v) Na-Deoxycholat, 0.02% (v/v) Nonidet P-40, washed with PBS and subsequently incubated in substrate solution (5 mM $K_3Fe(CN)_6$, 5 mM $K_4Fe(CN)_6$, 2 mM $MgCl_2$, in PBS containing 1 mg/ml (w/v) of the β-galactosidase substrate 5-bromo-4-chloro-indolyl-β-d-galactopyranoside (X-Gal) for 3 hours.

Electron microscopy and correlative electron/ light microscopy

After perfusion fixation with 4%PFA as described above, brains were further fixed for electron microscopy. For conventional electron microscopy, they were fixed with 2% glutaraldehyde in PB for 2 hours at 4°C, and postfixed with 2% osmium tetroxide (OsO_4) for 2 hours at 4°C. Specimens were dehydrated with graded ethanol and embedded in Epon812. For correlative light/electron microscopy, the specimens were cut into 30 μm sections with a vibratome (VT1200S, Leica Microsystems). Sections were immunolabeled with primary antibodies (cathepsin D, Shibata et al., 1998); LAMP1; Novus Biologicals; clone 1D4B) at 4°C over night. After washing with PBS, sections were incubated with secondary antibodies (anti-rabbit IgG Alexa Fluor 488 FluoroNanogold, Nanoprobes; anti-Rat IgG Cy3) and DAPI. Sections were then attached to a gridded glass-bottom dish (Matsunami) and observed with a confocal laser scanning microscope (TCS/SP5, Leica Microsystems). Sections were fixed in 2% glutaraldehyde in PBS for 1 hour at 4°C, and were subjected to gold enhancement using GoldEnhance Plus (Nanoprobes). Sections were postfixed, dehydrated, and embedded as described above. Embedded samples were cut at 80 nm with an ultramicrotome (UC6, Leica Microsystems), while ultrathin sections were stained with 4% uranyl acetate and 1% lead citrate. They were then examined with a transmission electron microscope (HT7700, Hitachi).

Immunohistochemical staining of neuromuscular junctions (NMJ)

Staining of NMJs was carried out as previously described (Dombert et al., 2014). Briefly, mice were deeply anesthetized and transcardially perfused with 4% PFA. Subsequently, the *orbicularis orbi* muscle was dissected and post-fixed in 4% PFA for at least two hours. The tissue was washed in PBS-T (0.1% Tween-20) for 20 minutes at RT and incubated with α-Bungarotoxin-Alexa488 (Invitrogen) for 25 minutes at RT. The tissue was then incubated overnight at 4°C with a blocking solution (2% BSA, 0.1% Tween-20 and 10% donkey serum), followed by incubation with the indicated primary antibodies for three days at 4°C. After washing with PBS at pH 7.4 (PAA Laboratories) three times for 15 minutes, the appropriate secondary antibodies were applied for 1 hour at RT. The tissue was washed again as above described, and embedded in Aqua Polymount (Polysciences).

IN VIVO LABELING WITH FLUORO-GOLD RETROGRADE TRACER

The application of the retrograde axonal tracer FluoroGold (FG; Fluorochrome) was previously described with minor modifications (Gey et al., 2016). Mice were injected with 4 x μl of FG (4% in H_2O) with a Hamilton syringe in the whisker pad. The animals were sacrificed and the brains were fixed in 4% PFA for one day and cut into 80 μm vibratome sections. For each animal, FG positive neurons of four sections were analyzed. Quantification was performed manually with ImageJ. All experiments were in accordance with institutional regulations by the local animal ethical committee (Regierungspräsidium Tübingen, Germany; TVA 1368).

Behavioral Studies

Eye blink reflex and whisker-orientation reflex

Facial nerve function was assessed by stimulation of facial movements (Crawley, 2007). The eye blink reflex was elicited by approaching the eye with the tip of a cotton swab. The whisker-orientation reflex was provoked by slightly stroking the whiskers

with a cotton swab tip, promoting an orientation response. Vigorousness of both responses was subsequently rated on a 3-point scale (0: absent – 1: reduced – 2: normal). The average of 6 assessments was used for analysis.

Whisker movement

Whisker movement was performed as described previously (Wanner et al., 2017). Prior to whisker movement analysis, mice were handled daily to accustom them for videotaping. For whisker movement analysis, all whiskers except the whiskers in the C row were clipped in anesthetized mice by micro scissors. Hand restraint mice were videotaped for 53 s by a high-speed camera at 100 Hz from top-view. Video sequences were reviewed and 1 s fragments were further processed in Templo Software (CONTEMPLAS GmbH, Germany). The selected video sequences were analyzed by Vicon Motus 2D software (CONTEMPLAS GmbH, Germany). The angular whisker position of the C1 whisker was determined by using a spatial model, consisting of a line between the fix points right and left eye and its corresponding midsagittal plane in a 90 degree angle. The plane for the whisker was set up by two points, the whisker shaft and a point on the vibrissae approximately 0.5 cm further out. The change of angle between the midsagittal plane and whisker was analyzed within 1 s for lesion and control side. The threshold for a peak was set to different angles (20°, 35°, 55° and 70°) and all angles for both pro- and retraction above these individual thresholds were summed up within these 100 Hz sequences (Figure 2). In addition, the peak numbers above these threshold angles were calculated in one 100 hs sequence counting one peak for each direction (Figure S4C). All experiments were in accordance with institutional regulations by the local animal ethical committee (Regierungspräsidium Tübingen, Germany; TVA 1368).

Grip strength, Balance Beam, Vertical pole, Rotarod

Forelimb grip strength was assessed by letting mice spontaneously grab a T-shaped bar connected to a digital dynamometer (Ugo Basile, Comerio, Italy). This allowed quantification of strength which was averaged over 10 trials. The rotarod test was included as a measure of motor coordination and equilibrium. All mice received 2 minutes of training at a fixed speed of 4 rpm on the apparatus (MED Associates Inc., St. Albans, Vermont, USA). Subsequently, 4 test trials (10 minutes intertrial interval) were conducted with an accelerating rotation from 4 to 40 rpm for 5 minutes. Drop latency was registered up to the 5 minutes cut-off. Motor function was further evaluated using the vertical pole test. Mice were positioned with their head upward on the top side of a vertical wooden beam, the surface of which was made rough with rope (length 55 cm, cross-section 1.5 cm). Latency to turn downward and descend was registered for every animal. Finally, the balance beam test was performed to gain further insight into sensorimotor function. Mice were trained to walk across a set of 1 m long narrow beams. Six beams were used which shape and diameter represented an increasing challenge for balance and equilibrium (square (SQ), cross-section: 28, 12 & 5 mm; round (RO), diameter: 28, 17 & 11 mm). Beams were placed 50 cm above the ground, terminating on a square escape platform. During the training phase, mice learned to traverse the 12 mm square beam until all subjects reached the predetermined criterion of 20 s traversal latency. The test phase consisted of 2 consecutive trials on each of the beams in the order described above. The average of both trials was used for analysis.

Plasmid construction and lentiviral production

FUW-Tmem106b-mCherry was generated by digestion of the FUWG plasmid by NheI and XbaI, and the resulting 10 kB fragment was purified by gel extraction. The cDNA of mCherry was amplified by PCR using the following primer: 5′- GCTGCTACCGGT GGAGGTGGT GGA TCTTCTGTGAGCAAGGGCGAGGAGGATAACATGG–3′ and 5′-GCTGCTTCTAGATTACTTGTACAGCTCGTCC –3′. The PCR product was purified, digested by AgeI and XbaI, and purified. The cDNA of *Tmem106b* was amplified by PCR using the following primer: 5′-GCTGCTGCTAGCACCATGGGAAAGTCTCTTTCTCACTTACC-3′and 5′-GCTGCTACCGGTTTGTTGTGGC TGAAGGACATTTAG-3′. The PCR product was purified, digested by NheI and AgeI, and again purified. Both fragments were simultaneously cloned into the FUGW backbone by ligation.

For the simultaneous expression of RFP-LC3 and Lamp1-GFP, we first constructed FUW-RFP-LC3. The FUGW plasmid was digested by XbaI and EcoRI, and the resulting 10 kB fragment was purified by gel extraction. pmRFP-LC3 (Addgene Plasmid #21075) was digested by NheI and EcoRI and the resulting 1.4 kB fragment was purified by gel extraction. Subsequently, both inserts were ligated into the XbaI and EcoRI sites of the backbone. The XbaI site was destroyed during cloning.

Next, FUW-RFP was digested by EcoRI, blunted, purified, and dephosphorylated. Lamp1-mGFP (Addegene Plasmid #34831) was digested by AseI and NotI, and the resulting CMV::Lamp1-mGFP fragment was purified by gel extraction, blunted and phosphorylated. Subsequently, both fragments were ligated to generate FUW-RFP-LC3-CMV::Lamp1-mGFP.

FUW-Lamp1-mGFP was generated by the digestion of FUGW by XbaI. The resulting 10kB fragment was purified by gel extraction, blunted and dephosphorylated. Lamp1-mGFP (Addegene Plasmid #34831) was digested by EcoRI and NotI and the resulting 2 kB fragment was purified by gel extraction, blunted and phosphorylated. Subsequently, both fragments were ligated.

Lentivirus was produced by co-transfecting HEK293T cells with the indicated expression and packaging plasmids using Lipofectamine 2000 (Invitrogen). The medium was replaced 24 hours after transfection and collected 24 hours later. Subsequently, the virus was concentrated by ultracentrifugation. For lentiviral transduction, MN were incubated with viral particles for 10 minutes at RT directly before plating.

Immunocytochemistry and live-cell imaging

Live-cell imaging: For live-cell imaging, 4,000 cells per cm^2 were plated on PORN/Laminin-coated coverslips and cultured for 7 days. On day 7, the cells were labeled with LysoTracker Green DND-26 (New England Biolabs) for 30 minutes and subsequently imaged for 7 minutes. The LysoTracker was applied in MN media without Phenol Red supplemented with BackDrop® Green Background

Suppressor (Cell Signaling). Lysosomal movement was monitored using an upright microscope (BXWI, Olympus), in a heated imaging chamber (Luigs & Neumann). Images (8-bit) were captured with a Rolera-XR camera (Qimaging) and StreamPix 4 software (Norpix) under continuous illumination with a 470 nm LED light source (Visitron Systems). Lysosomes moving less than 5 μm were considered as stationary or bidirectional moving, respectively.

Immunocytochemistry

For immunocytochemistry, we plated 4,000 cells per cm^2 and cultured the cells for 7 days. For stainings with LysoTracker, cells were labeled with LysoTracker Deep Red (Thermo Fisher Scientific) one hour prior to fixation. Subsequently, the cells were fixed with 4% PFA for 15 minutes at RT, followed by three washes with PBS for 5 minutes at RT. For blocking and permeabilization, the cells were incubated with blocking solution (10% Donkey Serum, 0.3% Triton X-100 in TBST) for 30 minutes at RT. Incubation with the primary antibody was carried out overnight at 4°C in the following solution: 1% Donkey Serum, 0.03% Triton X-100 in TBST. The next day, the cells were washed three times with TBST for 5 minutes at RT and the appropriate secondary antibodies were applied in TBST for 2 hours at RT. Finally, the MN were washed three times with TBST for 15 minutes. The cells were counterstained with DAPI during the first washing step after incubation with the secondary antibodies. The following primary antibodies were used: Cathepsin D (gift from Thomas Braulke, Claussen et al., 1997), Tuj1 (Neuromics, MO15013), LAMP1 (DSHB, Hybridoma Bank; clone 1D4B). Images were acquired using an Olympus Fluoview1000i confocal microscope.

FluoroGold endocytosis in primary MN

After five days in culture FluoroGold was added to the primary motoneurons at a final concentration of 0.01% (w/v) to the medium. After 15 or 60 minutes the cells were washed three times with PBS and then fixed with 4% PFA for 15 minutes at RT. The number of FluoroGold particles was analyzed using the ImageJ ''Analyze Particles'' plug-in. At least 90 cells were analyzed per genotype and time point.

Re-expression of TMEM106B

Expression of Tmem106b-mCherry in cultured MN: Primary MN were transduced with FUGW-Tmem106-mCherry and fixed with 4% PFA for 15 minutes at RT after 5 days in culture.

QUANTIFICATION AND STATISTICAL ANALYSIS

If not stated otherwise, a two-tailed unpaired t test was performed using GraphPad Prism Software Version 5.03. Significant values were considered at $p < 0.05$. Values are expressed as mean ± standard error of the mean (SEM) and significance is designated as *, $p < 0.05$; **, $p < 0.005$; ***, $p < 0.0001$.

Behavioral data are presented as mean + SEM. Shapiro-Wilk and Brown-Forsythe tests were used to determine normality and variance homogeneity. Violation of these assumptions was followed by non-parametric testing or (where possible) data transformation. Transformed data was retransformed for consistent visualization. Performance of *Tmem106b* wild-type, heterozygous and KO mice was compared using Kruskal-Wallis ANOVA on ranks (facial nerve reflexes), 1-way ANOVA (vertical pole, grip strength) and 2-way repeated-measures ANOVA (balance beam, rotarod). Dunn's and Holm-Sidak methods were used for multiple comparisons.

DATA AND CODE AVAILABILITY

No large datasets were produced in this study.